Astronomy
&
Astrophysics

Evidence of the accelerated expansion of the Universe from weak lensing tomography with COSMOS[⋆]

T. Schrabback[1,2], J. Hartlap[2], B. Joachimi[2], M. Kilbinger[3,4], P. Simon[5], K. Benabed[3], M. Bradač[6,7], T. Eifler[2,8],
T. Erben[2], C. D. Fassnacht[6], F. William High[9], S. Hilbert[10,2], H. Hildebrandt[1], H. Hoekstra[1], K. Kuijken[1],
P. J. Marshall[7,11], Y. Mellier[3], E. Morganson[11], P. Schneider[2], E. Semboloni[2,1], L. Van Waerbeke[12], and M. Velander[1]

[1] Leiden Observatory, Leiden University, Niels Bohrweg 2, 2333 CA Leiden, The Netherlands
   e-mail: schrabback@strw.leidenuniv.nl
[2] Argelander-Institut für Astronomie, Universität Bonn, Auf dem Hügel 71, 53121 Bonn, Germany
[3] Institut d'Astrophysique de Paris, CNRS UMR 7095 & UPMC, 98bis boulevard Arago, 75014 Paris, France
[4] Shanghai Key Lab for Astrophysics, Shanghai Normal University, Shanghai 200234, PR China
[5] The Scottish Universities Physics Alliance (SUPA), Institute for Astronomy, School of Physics, University of Edinburgh,
   Royal Observatory, Blackford Hill, Edinburgh EH9 3HJ, UK
[6] Physics Dept., University of California, Davis, 1 Shields Ave., Davis, CA 95616, USA
[7] Physics department, University of California, Santa Barbara, CA 93601, USA
[8] Center for Cosmology and AstroParticle Physics, The Ohio State University, Columbus, OH 43210, USA
[9] Department of Physics, Harvard University, Cambridge, MA 02138, USA
[10] Max Planck Institute for Astrophysics, Karl-Schwarzschild-Str. 1, 85741 Garching, Germany
[11] KIPAC, PO Box 20450, MS29, Stanford, CA 94309, USA
[12] University of British Columbia, Department of Physics and Astronomy, 6224 Agricultural Road, Vancouver,
   B.C. V6T 1Z1, Canada

ABSTRACT

We present a comprehensive analysis of weak gravitational lensing by large-scale structure in the *Hubble Space Telescope* Cosmic Evolution Survey (COSMOS), in which we combine space-based galaxy shape measurements with ground-based photometric redshifts to study the redshift dependence of the lensing signal and constrain cosmological parameters. After applying our weak lensing-optimized data reduction, principal-component interpolation for the spatially, and temporally varying ACS point-spread function, and improved modelling of charge-transfer inefficiency, we measured a lensing signal that is consistent with pure gravitational modes and no significant shape systematics. We carefully estimated the statistical uncertainty from simulated COSMOS-like fields obtained from ray-tracing through the Millennium Simulation, including the full non-Gaussian sampling variance. We tested our lensing pipeline on simulated space-based data, recalibrated non-linear power spectrum corrections using the ray-tracing analysis, employed photometric redshift information to reduce potential contamination by intrinsic galaxy alignments, and marginalized over systematic uncertainties. We find that the weak lensing signal scales with redshift as expected from general relativity for a concordance ΛCDM cosmology, including the full cross-correlations between different redshift bins. Assuming a flat ΛCDM cosmology, we measure $\sigma_8 (\Omega_{\rm m}/0.3)^{0.51} = 0.75 \pm 0.08$ from lensing, in perfect agreement with WMAP-5, yielding joint constraints $\Omega_{\rm m} = 0.266^{+0.025}_{-0.023}$, $\sigma_8 = 0.802^{+0.028}_{-0.029}$ (all 68.3% conf.). Dropping the assumption of flatness and using priors from the HST Key Project and Big-Bang nucleosynthesis only, we find a negative deceleration parameter q_0 at 94.3% confidence from the tomographic lensing analysis, providing independent evidence of the accelerated expansion of the Universe. For a flat wCDM cosmology and prior $w \in [-2, 0]$, we obtain $w < -0.41$ (90% conf.). Our dark energy constraints are still relatively weak solely due to the limited area of COSMOS. However, they provide an important demonstration of the usefulness of tomographic weak lensing measurements from space.

Key words. cosmological parameters – dark matter – large-scale structure of Universe – gravitational lensing: weak

1. Introduction

During the past decade strong evidence of an accelerated expansion of the Universe has been found with several independent cosmological probes including type Ia supernovae (Riess et al. 1998; Perlmutter et al. 1999; Riess et al. 2007; Kowalski et al. 2008; Hicken et al. 2009), cosmic microwave background (de Bernardis et al. 2000; Spergel et al. 2003;

Komatsu et al. 2009), galaxy clusters (Allen et al. 2008; Mantz et al. 2008, 2009; Vikhlinin et al. 2009), baryon acoustic oscillations (Eisenstein et al. 2005; Percival et al. 2007, 2009), integrated Sachs-Wolfe effect (Giannantonio et al. 2008; Granett et al. 2008; Ho et al. 2008), and strong gravitational lensing (Suyu et al. 2010). Within the standard cosmological framework, this can be described with the ubiquitous presence of a new constituent named dark energy, which counteracts the attractive force of gravity on the largest scales and contributes ~70% to the total energy budget today. There have been various attempts to explain dark energy, ranging from Einstein's cosmological constant, via a dynamic fluid named quintessence, to a

possible breakdown of general relativity (e.g. Huterer & Linder 2007; Albrecht et al. 2009), all of which lead to profound implications for fundamental physics. In order to make substantial progress and to be able to distinguish between the different scenarios, several large dedicated surveys are currently being designed.

One technique with particularly high promise for constraining dark energy (Albrecht et al. 2006; Peacock et al. 2006; Albrecht et al. 2009) is weak gravitational lensing, which utilizes the subtle image distortions imposed onto the observed shapes of distant galaxies, while their light bundles pass through the gravitational potential of foreground structures (e.g. Bartelmann & Schneider 2001). The strength of the lensing effect depends on the total foreground mass distribution, independent of the relative contributions of luminous and dark matter. It therefore provides a unique tool to study the statistical properties of large-scale structure directly (for reviews see Schneider 2006; Hoekstra & Jain 2008; Munshi et al. 2008).

Since its first detections by Bacon et al. (2000), Kaiser et al. (2000), Van Waerbeke et al. (2000) and Wittman et al. (2000), substantial progress has been made with the measurement of this cosmological weak lensing effect, which is also called cosmic shear. Larger surveys have significantly reduced statistical uncertainties (e.g. Hoekstra et al. 2002; Brown et al. 2003; Jarvis et al. 2003; Massey et al. 2005; Van Waerbeke et al. 2005; Hoekstra et al. 2006; Semboloni et al. 2006; Hetterscheidt et al. 2007; Fu et al. 2008), while tests on simulated data have led to better understanding of PSF systematics (Heymans et al. 2006a; Massey et al. 2007a; Bridle et al. 2010, and references therein). Finally, because it is a geometric effect, gravitational lensing depends on the source redshift distribution, where most earlier measurements have had to rely on external redshift calibrations from the small *Hubble* Deep Fields. Here, the impact of sampling variance was demonstrated by Benjamin et al. (2007), who recalibrated earlier measurements using photometric redshifts from the much larger CFHTLS-Deep, significantly improving derived cosmological constraints.

Dark energy affects the distance-redshift relation and suppresses the time-dependent growth of structures. Because it is sensitive to both effects, weak lensing is a powerful probe of dark energy properties, also providing important tests for theories of modified gravity (e.g. Benabed & Bernardeau 2001; Benabed & van Waerbeke 2004; Schimd et al. 2007; Doré et al. 2007; Jain & Zhang 2008; Schmidt 2008). Yet, in order to significantly constrain these redshift-dependent effects, the shear signal must be measured as a function of source redshift, an analysis often called weak lensing tomography or 3D weak lensing (e.g. Hu 1999, 2002; Huterer 2002; Jain & Taylor 2003; Heavens 2003; Hu & Jain 2004; Bernstein & Jain 2004; Simon et al. 2004; Takada & Jain 2004; Heavens et al. 2006; Taylor et al. 2007). Redshift information is additionally required to eliminate potential contamination of the lensing signal from intrinsic galaxy alignments (e.g. King & Schneider 2002; Hirata & Seljak 2004; Heymans et al. 2006b; Joachimi & Schneider 2008). In general, weak lensing studies have to rely on photometric redshifts (e.g. Benitez 2000; Ilbert et al. 2006; Hildebrandt et al. 2008), given that most of the studied galaxies are too faint for spectroscopic measurements.

So far, tomographic cosmological weak lensing techniques have been applied to real data by Bacon et al. (2005), Semboloni et al. (2006), Kitching et al. (2007) and Massey et al. (2007c). Dark energy constraints from previous weak lensing surveys were limited by the lack of the required individual photometric redshifts (Jarvis et al. 2006; Hoekstra et al. 2006;

Semboloni et al. 2006; Kilbinger et al. 2009a) or small survey area (Kitching et al. 2007). The currently best data set for 3D weak lensing is given by the COSMOS Survey (Scoville et al. 2007a), which is the largest continuous area ever imaged with the *Hubble Space Telescope* (HST), comprising 1.64 deg^2 of deep imaging with the Advanced Camera for Surveys (ACS). Compared to ground-based measurements, the HST point-spread function (PSF) yields substantially increased number densities of sufficiently resolved galaxies and better control of systematics due to smaller PSF corrections. Although HST has been used for earlier cosmological weak lensing analyses (e.g. Refregier et al. 2002; Rhodes et al. 2004; Miralles et al. 2005; Heymans et al. 2005; Schrabback et al. 2007), these studies lack the area and deep photometric redshifts that are available for COSMOS (Ilbert et al. 2009). This combination of superb space-based imaging and ground-based photometric redshifts makes COSMOS the perfect test case for 3D weak lensing studies. Massey et al. (2007c) conducted an earlier 3D weak lensing analysis of COSMOS, in which they correlated the shear signal between three redshift bins and constrained the matter density Ω_m and power spectrum normalization σ_8. In this paper we present a new analysis of the data, with several differences compared to the earlier study: we employ a new, exposure-based model for the spatially and temporally varying ACS PSF, which has been derived from dense stellar fields using a principal component analysis (PCA). Our new parametric correction for the impact of charge transfer inefficiency (CTI) on stellar images eliminates earlier PSF modelling uncertainties caused by confusion of CTI- and PSF-induced stellar ellipticity. Using the latest photometric redshift catalogue of the field (Ilbert et al. 2009), we split our galaxy sample into five individual redshift bins and also estimate the redshift distribution for very faint galaxies forming a sixth bin without individual photometric redshifts, doubling the number of galaxies used in our cosmological analysis. We study the redshift scaling of the shear signal between these six bins in detail, employ an accurate covariance matrix obtained from ray-tracing through the Millennium Simulation, which we also use to recalibrate non-linear power spectrum corrections, and marginalize over parameter uncertainties. In addition to Ω_m and σ_8, we also constrain the dark energy equation of state parameter w for a flat wCDM cosmology, and the vacuum energy density Ω_Λ for a general (non-flat) ΛCDM cosmology, yielding constraints for the deceleration parameter q_0.

This paper is organized as follows. We summarize the most important information on the data and photometric redshift catalogue in Sect. 2, while further details on the ACS data reduction are given in Appendix A. Section 3 summarizes the weak lensing measurements including our new correction schemes for PSF and CTI, for which we provide details in Appendix B. We conduct various tests for shear-related systematics in Sect. 4. We then present the weak lensing tomography analysis in Sect. 5, and cosmological parameter estimation in Sect. 6. We discuss our findings and conclude in Sect. 7.

Throughout this paper all magnitudes are given in the AB system, where i_{814} denotes the SExtractor (Bertin & Arnouts 1996) MAG_AUTO magnitude measured from the ACS data (Sect. 2.1), while i^+ is the MAG_AUTO magnitude determined by Ilbert et al. (2009) from the Subaru data (Sect. 2.2.1). In several tests we employ a reference WMAP-5-like (Dunkley et al. 2009) flat ΛCDM cosmology characterized by $\Omega_m = 0.25$, $\sigma_8 = 0.8$, $h = 0.72$, $\Omega_b = 0.044$, $n_s = 0.96$, where we use the transfer function by Eisenstein & Hu (1998) and non-linear power spectrum corrections according to Smith et al. (2003).

2. Data

2.1. HST/ACS data

The COSMOS Survey (Scoville et al. 2007a) is the largest contiguous field observed with the *Hubble Space Telescope*, spanning a total area of $\sim 77' \times 77'$ (1.64 deg^2). It comprises 579 ACS tiles, each observed in F814W for 2028 s using four dithered exposures. The survey is centred at $\alpha = 10^h00^m28.6^s$, $\delta = +02°12'21''.0$ (J2000.0), and data were taken between October 2003 and November 2005.

We have reduced the ACS/WFC data starting from the flat-fielded images. We apply updated bad pixel masks, subtract the sky background, and compute optimal weights as detailed in Appendix A. For the image registration, distortion correction, cosmic ray rejection, and stacking we use MultiDrizzle[1] (Koekemoer et al. 2002), applying the latest time-dependent distortion solution from Anderson (2007). We iteratively align exposures within each tile by cross-correlating the positions of compact sources and applying residual shifts and rotations.

In tests with dense stellar fields we found that the default cosmic ray rejection parameters of MultiDrizzle can lead to false flagging of central stellar pixels as cosmic rays, especially if telescope breathing introduces significant PSF variations (see Sect. 3) between combined exposures. Thus, stars will be partially rejected in exposures with deviating PSF properties. On the contrary, galaxies will not be flagged due to their shallower light profiles, leading to different effective stacked PSFs for stars and galaxies. To avoid any influence on the lensing analysis, we create separate stacks for the shape measurement of galaxies and stars, where we use close to default cosmic ray rejection parameters for the former (driz_cr_snr="4.0   3.0", driz_cr_scale="1.2   0.7", see Koekemoer et al. 2002, 2007), but less aggressive masking for the latter (driz_cr_snr="5.0   3.0", driz_cr_scale="3.0 0.7"). As a result, the false masking of stars is substantially reduced. On the downside some actual cosmic rays lead to imperfectly corrected artifacts in the "stellar" stacks. This is not problematic given the very low fraction of affected stars, for which the artifacts only introduce additional noise in the shape measurement.

For the final image stacking we employ the LANCZOS3 interpolation kernel and a pixel scale of $0''.05$, which minimizes noise correlations and aliasing without unnecessarily broadening the PSF (for a detailed comparison to other kernels see Jee et al. 2007). Based on our input noise models (see Appendix A) we compute a correctly scaled rms image for the stack. We match the stacked image WCS to the ground-based catalogue by Ilbert et al. (2009).

We employ our rms noise model for object detection with SExtractor (Bertin & Arnouts 1996), where we require a minimum of 8 adjacent pixels being at least 1.4σ above the background, employ deblending parameters DEBLEND_NTHRESH = 32, DEBLEND_MINCONT = 0.01, and measure MAG_AUTO magnitudes i_{814}, which we correct for a mean galactic extinction offset of 0.035 (Schlegel et al. 1998). Objects near the field boundaries or containing noisy pixels, for which fewer than two good input exposures contribute, are automatically excluded. We also create magnitude-scaled polygonal masks for saturated stars and their diffraction spikes. Furthermore, we reject scattered light and large, potentially incorrectly deblended galaxies by running SExtractor with a low 0.5σ detection threshold for 3960 adjacent pixels, where we

further expand each object mask by six pixels. The combined masks for the stacks were visually inspected and adapted if necessary.

Our fully filtered mosaic shear catalogue contains a total of 446 934 galaxies with $i_{814} < 26.7$, corresponding to 76 galaxies/arcmin^2, where we exclude double detections in overlapping tiles and reject the fainter component in the case of close galaxy pairs with separations $< 0''.5$. For details on the weak lensing galaxy selection criteria see Appendix B.6.

In addition to the stacked images, our fully time-dependent PSF analysis (see Sect. 3, Appendix B.5) makes use of individual exposures, for which we use the cosmic ray-cleansed *COR* images before resampling, provided by MultiDrizzle during the run with less aggressive cosmic ray masking. These are only used for the analysis of high signal-to-noise stars, which can be identified automatically in the half-light radius versus signal-to-noise space[2]. Here we employ simplified field masks only excluding the outer regions of a tile with poor cosmic ray masking.

2.2. Photometric redshifts

2.2.1. Individual photometric redshifts for $i^+ < 25$ galaxies

We use the public COSMOS-30 photometric redshift catalogue from Ilbert et al. (2009), which covers the full ACS mosaic and is magnitude limited to $i^+ < 25$ (Subaru SExtractor MAG_AUTO magnitude). It is based on the 30 band photometric catalogue, which includes imaging in 20 optical bands, as well as near-infrared and deep IRAC data (Capak et al. 2009, in preparation). Ilbert et al. (2009) computed photometric redshifts using the *Le Phare* code (S. Arnouts & O. Ilbert; also Ilbert et al. 2006), reaching an excellent accuracy of $\sigma_{\Delta z/(1+z)} = 0.012$ for $i^+ < 24$ and $z < 1.25$. The near-infrared (NIR) and infrared coverage extends the capability for reliable photo-z estimation to higher redshifts, where the Balmer break moves out of the optical bands. Extended to $z \sim 2$, Ilbert et al. (2009) find an accuracy of $\sigma_{\Delta z/(1+z_s)} = 0.06$ at $i^+ \sim 24$. The comparison to spectroscopic redshifts from the zCOSMOS-deep sample (Lilly et al. 2007) with $i^+_{median} = 23.8$ indicates a 20% catastrophic outlier rate (defined as $|z_{phot} - z_{spec}|/(1 + z_{spec}) > 0.15$) for galaxies at $1.5 < z_{spec} < 3$. In particular, for 7% of the high-redshift ($z_{spec} > 1.5$) galaxies a low-redshift photo-z ($z_{phot} < 0.5$) was assigned. This degeneracy is expected for faint ($i^+ \gtrsim 24$) high-redshift galaxies, for which the Balmer break cannot be identified if they are undetected in the NIR data (limiting depth $J \sim 23.7$, $K \sim 23.7$ at 5σ). Due to the employed magnitude prior the contamination is expected to be mostly uni-directional from high to low redshifts.

We tested this by comparing the COSMOS-30 catalogue to photometric redshifts estimated by Hildebrandt et al. (2009) in the overlapping CFHTLS-D2 field using only optical u^*griz bands and the *BPZ* photometric redshift code (Benitez 2000). Here we indeed find that 56% of the matched $i^+ < 25$ galaxies with COSMOS-30 photo-zs in the range $2 \leq z_{C30} \leq 4$ are identified at $z_{D2} \leq 0.6$ in the D2 catalogue, if only a weak cut to reject galaxies with double-peaked D2 photo-z PDFs (ODDS > 0.7) is applied[3].

---

[1] MultiDrizzle version 3.1.0.

[2] $\Delta r_h = 0.25$ pixel wide kernel; $S/N > 20$, defined as in Erben et al. (2001); peak flux $<25\,000$ e$^-$.

[3] A more stringent cut ODDS > 0.95 reduces this fraction to 14%. Yet, it also reduces the absolute number of galaxies by a factor 4.7. Note that, in contrast, 26% (22%) of the matched galaxies with a D2 photo-z $2 \leq z_{D2} \leq 4$ are placed at $z_{C30} \leq 0.6$ for ODDS > 0.7 (ODDS > 0.95). These could be explained by Lyman-break galaxies, which are better

If not accounted for, such a contamination of a low-photo-z sample with high-redshift galaxies would be particularly severe for weak lensing tomography, given the strong dependence of the lensing signal on redshift. In Sect. 5 we will therefore split galaxies with assigned $z_{phot} < 0.6$ into sub-samples with expected low ($i^+ < 24$) and high ($i^+ > 24$) contamination, where we only include the former in the cosmological analysis. Matching our shear catalogue to the fully masked COSMOS-30 photo-z catalogue yields a total of 194 976 unique matches.

2.2.2. Estimating the redshift distribution for $i^+ > 25$ galaxies

In order to include galaxies without individual photo-zs in our analysis, we need to estimate their redshift distribution. Figure 1 shows the mean photometric COSMOS-30 redshift for galaxies in our shear catalogue as a function of i_{814}. In the whole magnitude range $23 < i_{814} < 25$ the data are very well described by the relation

$$\langle z \rangle = (0.276 \pm 0.003)(i_{814} - 23) + 0.762 \pm 0.003. \quad (1)$$

For comparison we also plot points from the *Hubble* Deep Field-North (HDF-N, Fernández-Soto et al. 1999) and *Hubble* Ultra Deep Field (HUDF, Coe et al. 2006)[4] for the extended magnitude range $23 < i_{814} < 27$, where both catalogues are redshift complete. The HDF-N data agree very well with the COSMOS fit over the whole extended range, on average to 2%. In contrast, the mean photometric redshifts in the HUDF are on average higher than (1) by 16% for $23 < i_{814} < 25$ and 10% for $25 < i_{814} < 27$. The difference between the HDF-N and HUDF can be regarded as a rough estimate for the impact of sampling variance in such small fields. The fact that the HUDF galaxies systematically deviate from (1) not only for $i_{814} > 25$ but *also* for $i_{814} < 25$ where COSMOS-30 photo-zs are available, indicates that it is most likely affected by sampling variance containing a relative galaxy over-density at higher redshift. Given the excellent fit for the COSMOS galaxies and very good agreement for the HDF-N data we are thus confident to use (1) for a limited extrapolation to $i_{814} < 26.7$ for our shear galaxies. This is also motivated by the fact that $i_{814} < 25$ and $i_{814} > 25$ galaxies are not completely independent, but partially probe the same large-scale structure at different luminosities.

Due to the non-linear dependence of the shear signal on redshift it is not only necessary to estimate the correct mean redshift of the galaxies, but also their actual redshift distribution. In weak lensing studies the redshift distribution is often parametrized as $p(z) \propto (z/z_0)^\alpha \exp\left[-(z/z_0)^\beta\right]$ (e.g. Brainerd et al. 1996), which Schrabback et al. (2007) extended by fitting α, β in combination with a linear dependence of the median redshift on magnitude, leading to a magnitude-dependent z_0. Yet, it was noted that this fit was not fully capable to reproduce the shape of the redshift distribution of the fitted galaxies. Given the higher accuracy needed for the analysis of the larger COSMOS Survey we use a modified parametrization

$$p(z|i_{814}) \propto \left(\frac{z}{z_0}\right)^\alpha \left(\exp\left[-\left(\frac{z}{z_0}\right)^\beta\right] + cu^d \exp\left[-\left(\frac{z}{z_0}\right)^\gamma\right]\right), \quad (2)$$

constrained by the deeper u^* observations in the CFHTLS-D2. In any case we expect negligible influence on our results given our treatment for faint $z_{C30} \leq 0.6$ galaxies.

[4] For the HUDF we interpolate i_{814} from the i_{775} and z_{850} magnitudes provided in the Coe et al. (2006) catalogue.
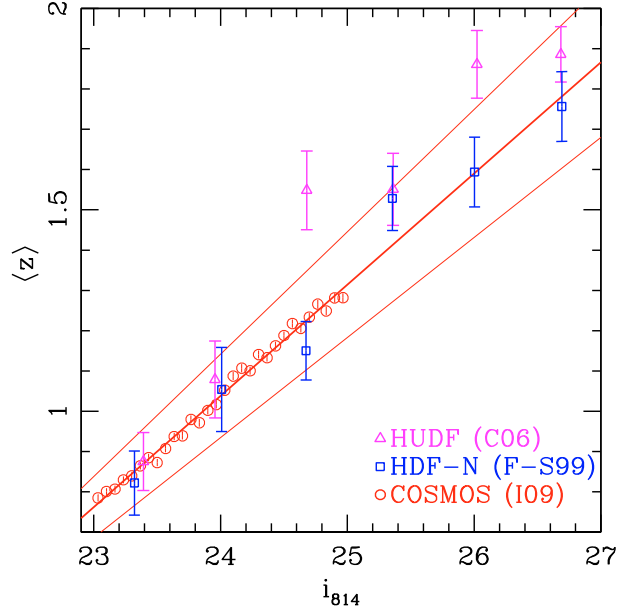
Fig. 1. Relation between the mean photometric redshift and i_{814} magnitude for COSMOS, HUDF, and HDF-N, where the error-bars indicate the error of the mean assuming Gaussian scatter and neglecting sampling variance. The best fit (1) to the COSMOS data from $i_{814} < 25$ is shown as the bold line, whereas the thin lines indicate the conservative 10% uncertainty considered for the extrapolation in the cosmological analysis. The HDF-N data agree with the relation very well, whereas the mean redshifts are higher in the HUDF both for $i_{814} < 25$ and $i_{814} > 25$, demonstrating the influence of sampling variance in such small fields.

where $z_0 = z_0(i_{814})$, and $u = \max[0, (i_{814} - 23)]$. Using a maximum likelihood fit[5] we determine best-fitting parameters $(\alpha, \beta, c, d, \gamma) = (0.678, 5.606, 0.581, 1.851, 1.464)$ from the individual magnitudes, photo-zs, and (symmetric) 68% photo-z errors of all galaxies with $23 < i_{814} < 25$. From Eqs. (1) and (2) we then numerically compute the non-linear relation between z_0 and i_{814}, for which we provide the fitting formulae

$$z_0 = 0.446(i_{814} - 23) + 1.235 \quad \text{for} \quad 22 < i_{814} \leq 23 \quad (3)$$

$$z_0 = \sum_{j=0}^{j=7} a_j[(i_{814} - 23)/4]^j \quad \text{for} \quad 23 < i_{814} < 27 \quad (4)$$

with $(a_0, ..., a_7) = (1.237, 1.691, -12.167, 43.591, -76.076, 72.567, -35.959, 7.289)$. The total redshift distribution of the survey is then simply given by the mean distribution $\phi(z) = \sum_{k=1}^{N} p(z|i_{814,k})/N$.

We chose the functional form of (2) because its first addend allows for a good description of the peak of the redshift distribution, while the second addend fits the magnitude-dependent tail at higher redshifts; see Fig. 2 for a comparison of the data and model in four magnitude bins. In Fig. 3 we compare the actual redshift distribution for the combined HDF-N and HUDF data to the one we *predict* from their magnitude distribution and the fit to the COSMOS data, finding very good agreement also for $25 < i_{814} < 27$. The only major deviation is given by a galaxy over-density in the HUDF photo-z data near $z \sim 3.2$, which is also partially responsible for the higher mean redshift in Fig. 1 and which may be attributed to large-scale structure.

Our fitting scheme assumes that the COSMOS-30 photo-zs provide unbiased estimates for the true galaxy redshifts.

[5] We employ the CERN Program Library MINUIT (http://wwwasdoc.web.cern.ch/wwwasdoc/minuit/).
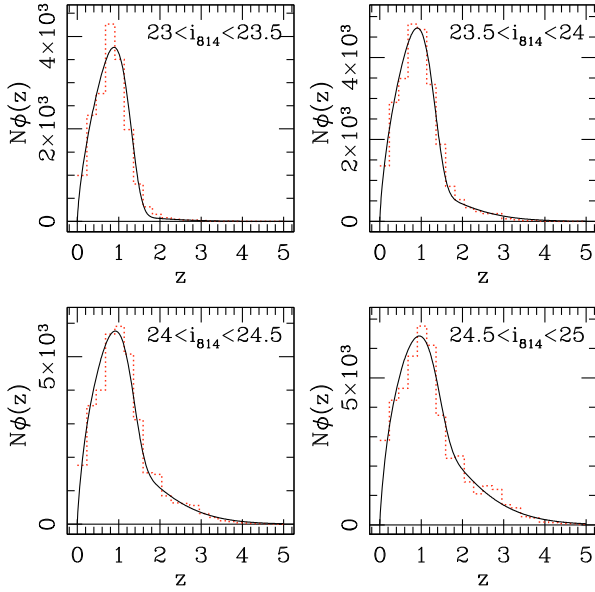
Fig. 2. Redshift histogram for galaxies in our shear catalogue with COSMOS-30 photo-zs (dotted), split into four magnitude bins. The solid curves show the fit according to (1) and (2), which is capable to describe both the peak and high redshift tail.
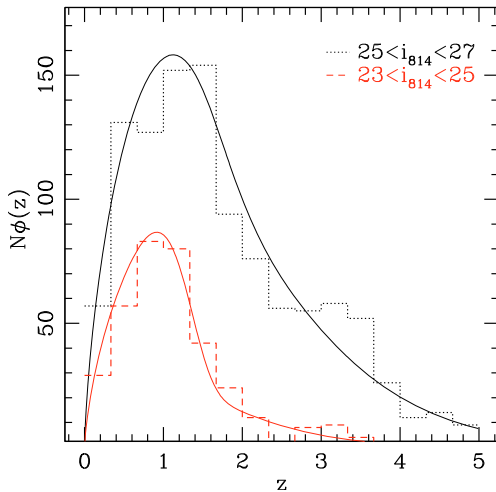

Fig. 3. Combined redshift histogram for the HDF-N and HUDF photo-zs, split into two magnitude bins. The solid curves show the prediction according to (1), (2) and the galaxy magnitude distribution. The good agreement for $25 < i_{814} < 27$ galaxies confirms the applicability of the model in this magnitude regime.

However, in Sect. 2.2 we suspected that $i^+ \gtrsim 24$ galaxies with assigned $z < 0.6$ might contain a significant contamination with high-redshift galaxies. To assess the impact of this uncertainty, we derive the fits for (1) and (2) using only galaxies with $23 < i^+ < 24$, reducing the estimated mean redshift of shear galaxies without COSMOS-30 photo-z by 4%. As an alternative test, we assume that 20% of the $z < 0.6$ galaxies with $24 < i^+ < 25$ are truly at $z = 2$, increasing the estimated mean redshift by 8%. Compared to the fit uncertainty in (1) ($\sim$1%) this constitutes the main source of error for our redshift extrapolation. In the cosmological parameter estimation (Sect. 6), we constrain this uncertainty and marginalize over it using a nuisance parameter, which rescales the redshift distribution within a conservatively chosen $\pm 10\%$ interval. Note that the +4% difference between the measured and predicted mean redshift of the

combined HDF-N and HUDF data in Fig. 3 actually suggests a smaller uncertainty.

3. Weak lensing shape measurements

To measure an accurate lensing signal, we have to carefully correct for instrumental signatures. Even with the high-resolution space-based data at hand, we have to accurately account for both PSF blurring and ellipticity, which introduce spurious shape distortions. To do so, one requires both a good model for the PSF, and a method which accurately employs it to measure unbiased estimates for the (reduced) gravitational shear g from noisy galaxy images.

For the latter, we use the KSB+ formalism (Kaiser et al. 1995; Luppino & Kaiser 1997; Hoekstra et al. 1998), see Erben et al. (2001), Schrabback et al. (2007) and Appendix B.1 for details on our implementation. As found with simulations of ground-based weak lensing data, KSB+ can significantly underestimate gravitational shear (Erben et al. 2001; Bacon et al. 2001; Heymans et al. 2006a; Massey et al. 2007a), where the calibration bias m and possible PSF anisotropy residuals c, defined via

$$g^{\mathrm{obs}} - g^{\mathrm{true}} = m g^{\mathrm{true}} + c, \qquad (5)$$

depend on the details of the implementation. Massey et al. (2007a, STEP2) detected a shear measurement degradation for faint objects for our pipeline, which is not surprising given the fact that the KSB+ formalism does not account for noise. While Schrabback et al. (2007) simply corrected for the resulting mean calibration bias, the 3D weak lensing analysis performed here requires unbiased shape measurements not only on average, but also as function of redshift, and hence galaxy magnitude and size (see e.g. Kitching et al. 2008, 2009; Semboloni et al. 2009). We therefore empirically account for this degradation with a power-law fit to the signal-to-noise dependence of the calibration bias

$$m = -0.078 \left(\frac{S/N}{2} \right)^{-0.38}, \qquad (6)$$

where S/N is computed with the galaxy size-dependent KSB weight function (Erben et al. 2001), and corrected for noise correlations as done in Hartlap et al. (2009). As S/N relates to the significance of the galaxy shape measurement, it provides a more direct correction for noise-related bias than fits as a function of magnitude or size. We have determined this correction using the STEP2 simulations of ground-based weak lensing data (Massey et al. 2007a). In order to test if it performs reliably for the ACS data, we have analysed a set of simulated ACS-like data (see Appendix B.2). In summary, we find that the remaining calibration bias is $m = +0.008 \pm 0.002$ on average, and $|m| < 0.02$ over the entire magnitude range used, which is negligible compared to the statistical uncertainty for COSMOS. Likewise, PSF anisotropy residuals, which are characterized in (5) by c, are found to be negligible in the simulation (dispersion $\sigma_c = 0.0006$), assuming accurate PSF interpolation.

Weak lensing analyses usually create PSF models from the observed images of stars, which have to be interpolated for the position of each galaxy. Typically, a high galactic latitude ACS field contains only $\sim$10−20 stars with sufficient S/N, which are too few for the spatial polynomial interpolation commonly used in ground-based weak lensing studies. In addition, a stable PSF model cannot be used, given that substantial temporal PSF variations have been detected, mostly caused by focus changes resulting from orbital temperature variations (telescope breathing),

mid-term seasonal effects, and long-term shrinkage of the optical telescope assembly (OTA) (e.g. Krist 2003; Lallo et al. 2006; Anderson & King 2006; Schrabback et al. 2007; Rhodes et al. 2007). To circumvent this problem, we have implemented a PSF correction scheme based on principal component analysis (PCA), as first suggested by Jarvis & Jain (2004). We have analysed 700 i_{814} exposures of dense stellar fields, interpolated the PSF variation in each exposure with polynomials, and performed a PCA analysis of the polynomial coefficient variation. We find that ~97% of the total PSF ellipticity variation in random pointings can be described with a single parameter related to the change in telescope focus, confirming earlier results (e.g. Rhodes et al. 2007). However, we find that additional variations are still significant. In particular, we detect a dependence on the relative angle between the pointing and the orbital telescope movement[6], suggesting that heating in the sunlight does not only change the telescope focus, but also creates slight additional aberrations dependent on the relative sun angle. These deviations may be coherent between COSMOS tiles observed under similar orbital conditions. To account for this effect, we split the COSMOS data into 24 epochs of observations taken closely in time, and determine a low-order, focus-dependent residual model from all stars within one epoch. We provide further details on our PSF correction scheme in Appendix B.5.

As an additional observational challenge, the COSMOS data suffer from defects in the ACS CCDs, which are caused by the continuous cosmic ray bombardment in space. These defects act as charge traps reducing the charge-transfer-efficiency (CTE), an effect referred to as charge-transfer-inefficiency (CTI). When the image of an object is transferred across such a defect during parallel read-out, a fraction of its charge is trapped and statistically released, effectively creating charge-trails following objects in the read-out y-direction (e.g. Rhodes et al. 2007; Chiaberge et al. 2009; Massey et al. 2010). For weak lensing measurements the dominant effect of CTI is the introduction of a spurious ellipticity component in the read-out direction. In contrast to PSF effects, CTI affects objects non-linearly due to the limited depth of charge traps. Thus, the two effects must be corrected separately. As done by Rhodes et al. (2007), we employ an empirical correction for galaxy shapes, but also take the dependence on sky background into account. Making use of the CTI flux-dependence, we additionally determine and apply a parametric CTI model for stars, which is important as PSF and CTI-induced ellipticity get mixed otherwise. We present details on our CTI correction schemes for stars in Appendix B.4 and for galaxies in Appendix B.6. Note that Massey et al. (2010) recently presented a method to correct for CTI directly on the image level. We find that the methods employed here are sufficient for our science analysis, as also confirmed by the tests presented in Sect. 4. However, for weak lensing data with much stronger CTE degradation, such as ACS data taken after Servicing Mission 4, their pixel-based correction should be superior.

4. 2D shear-shear correlations and tests for systematics

To measure the cosmological signal and conduct tests for systematics we compute the second-order shear-shear correlations

$$\xi_{\pm}(\theta) = \frac{\sum_{i,j}(\gamma_{t,i}\gamma_{t,j} \pm \gamma_{\times,i}\gamma_{\times,j})\Delta_{ij}}{\sum_{i,j}\Delta_{ij}} \quad (7)$$

[6] Technically speaking, we show a dependence on the velocity aberration plate scale factor in Fig. B.6.

from galaxy pairs separated by $\vartheta = |\boldsymbol{\vartheta}_i - \boldsymbol{\vartheta}_j|$. Here, $\Delta_{ij} = 1$ if the galaxy separation ϑ falls within the considered angular bin around θ, and $\Delta_{ij} = 0$ otherwise. In (7) we approximate our reduced shear estimates $g = \gamma/(1 - \kappa) \simeq \gamma$ with the shear γ as commonly done in cosmological weak lensing (typically $|\kappa| \sim 1\%-3\%$; correction employed in Sect. 6.4), decompose it into the tangential component γ_t and the 45 degree rotated cross-component $\gamma_{\times}$ relatively to the separation vector, and employ uniform weights.

As an important consistency check in weak gravitational lensing, the signal can be decomposed into a curl-free component (E-mode) and a curl component (B-mode). Given that lensing creates only E-modes, the detection of a significant B-mode indicates the presence of uncorrected residual systematics in the data. Crittenden et al. (2002) show that $\xi_{\pm}$ can be decomposed into E- and B-modes as

$$\xi_{E/B}(\theta) = \frac{\xi_+(\theta) \pm \xi'(\theta)}{2}, \quad (8)$$

with

$$\xi'(\theta) = \xi_-(\theta) + 4 \int_\theta^\infty \frac{d\vartheta}{\vartheta}\xi_-(\vartheta) - 12\theta^2 \int_\theta^\infty \frac{d\vartheta}{\vartheta^3}\xi_-(\vartheta). \quad (9)$$

We plot this decomposition for our COSMOS catalogue in the left panel of Fig. 4. Given that the integration in (9) extends to infinity, we employ ΛCDM predictions for $\theta > 40'$, leading to a slight model-dependence, which is indicated by the dashed curves corresponding to $\sigma_8 = (0.7, 0.9)$, whereas the points have been computed for $\sigma_8 = 0.8$. Within this section, error-bars and covariances are estimated from 300 bootstrap resamples of our galaxy shear catalogue, which accounts for both shot noise and shape noise. As seen in Fig. 4, we detect no significant B-mode ξ_B. However, note that different angular scales are highly correlated for $\xi_{E/B}$, which mixes power on a broad range of scales and potentially smears out the signatures of systematics.

An E/B-mode decomposition, for which the correlation between different scales is weaker, is provided by the dispersion of the aperture mass (Schneider 1996)

$$\langle M^2_{ap/\perp}\rangle(\theta) = \frac{1}{2}\int_0^{2\theta}\frac{d\vartheta\,\vartheta}{\theta^2}\left[\xi_+(\vartheta)T_+\left(\frac{\vartheta}{\theta}\right) \pm \xi_-(\vartheta)T_-\left(\frac{\vartheta}{\theta}\right)\right], \quad (10)$$

with $T_{\pm}$ given in Schneider et al. (2002), where we employ the aperture mass weight function proposed by Schneider et al. (1998). The computation of (10) requires integration from zero, which is not practical for real data. We therefore truncate $\xi_{\pm}$ for $\theta < 0.'05$, where the introduced bias is small compared to our statistical errors (Kilbinger et al. 2006). Massey et al. (2007c) measure a significant B-mode component $\langle M^2_\perp\rangle$ at scales $1' \lesssim \theta \lesssim 3'$, whereas this signal is negligible in the present analysis. We quantify the on average slightly positive $\langle M^2_\perp\rangle$ by fitting a mean offset taking the bootstrap covariance into account (correlation between neighbouring points $\simeq 0.5$), yielding an average $\overline{\langle M^2_\perp\rangle} = (1 \pm 4) \times 10^{-7}$ if all points are considered, and $\overline{\langle M^2_\perp\rangle}(\theta < 6') = (1.0 \pm 1.4) \times 10^{-6}$ or $\overline{\langle M^2_\perp\rangle}(\theta < 2') = (4.0 \pm 4.7) \times 10^{-6}$ if only small scales are included, consistent with no B-modes.

The cleanest E/B-mode decomposition is given by the ring statistics (Schneider & Kilbinger 2007; Eifler et al. 2010; see also Fu & Kilbinger 2010), which can be computed from the correlation function using a finite interval with non-zero lower integration limit

$$\langle \mathcal{RR}\rangle_{E/B}(\Psi) = \frac{1}{2}\int_{\eta\Psi}^{\Psi}\frac{d\vartheta}{\vartheta}\left[\xi_+(\vartheta)Z_+(\vartheta, \eta) \pm \xi_-(\vartheta)Z_-(\vartheta, \eta)\right], \quad (11)$$
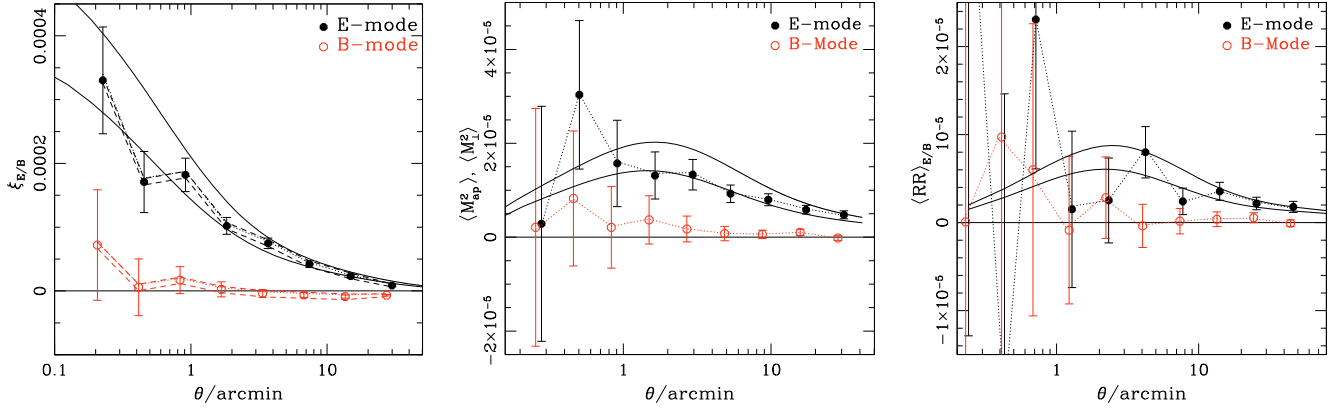
Fig. 4. Decomposition of the shear field into E- and B-modes using the shear correlation function $\xi_{E/B}$ (*left*), aperture mass dispersion $\langle M^2_{ap/\perp} \rangle$ (*middle*), and ring statistics $\langle \mathcal{RR} \rangle_{E/B}$ (*right*). Error-bars have been computed from 300 bootstrap resamples of the shear catalogue, accounting for shape and shot noise, but not for sampling variance. The solid curves indicate model predictions for $\sigma_8 = (0.7, 0.8)$. In all cases the B-mode is consistent with zero, confirming the success of our correction for instrumental effects. For $\xi_{E/B}$ the E/B-mode decomposition is model-dependent, where we have assumed $\sigma_8 = 0.8$ for the points, while the dashed curves have been computed for $\sigma_8 = (0.7, 0.9)$. The dotted curves indicate the signal if the residual ellipticity correction discussed in Appendix B.6 is not applied, yielding nearly unchanged results. Note that the correlation between points is strongest for $\xi_{E/B}$ and weakest for $\langle \mathcal{RR} \rangle_{E/B}$.

with functions $Z_\pm$ given in Schneider & Kilbinger (2007). We compute $\langle \mathcal{RR} \rangle_{E/B}$ using a scale-dependent integration limit η as outlined in Eifler et al. (2010). As can be seen from the right panel of Fig. 4, also $\langle \mathcal{RR} \rangle_B$ is consistent with no B-mode signal.

The non-detection of significant B-modes in our shear catalogue is an important confirmation for our correction schemes for instrumental effects and suggests that the measured signal is truly of cosmological origin.

As a final test for shear-related systematics we compute the correlation between corrected galaxy shear estimates γ and uncorrected stellar ellipticities e^*

$$\xi^{\mathrm{sys}}_{tt/\times\times}(\theta) = \frac{\langle \gamma_{t/\times} e^*_{t/\times} \rangle |\langle \gamma_{t/\times} e^*_{t/\times} \rangle|}{\langle e^*_{t/\times} e^*_{t/\times} \rangle}, \tag{12}$$

which we normalize using the stellar auto-correlation as suggested by Bacon et al. (2003). As detailed in Appendix B.6, we employ a somewhat ad hoc residual correction for a very weak remaining instrumental signal. We find that ξ^{sys} is indeed only consistent with zero if this correction is applied (Fig. 5), yet even without correction, ξ^{sys} is negligible compared to the expected cosmological signal. The negligible impact can also be seen from the two-point statistics in Fig. 4, where the points are computed including residual correction, while the dotted lines indicate the measurement without it. We suspect that this residual instrumental signature could either be caused by the limited capability of KSB+ to fully correct for a complex space-based PSF, or a residual PSF modelling uncertainty due to the low number of stars per ACS field. In any case we have verified that this residual correction has a negligible impact on the cosmological parameter estimation in Sect. 6, changing our constraints on σ_8 at the 2% level, well within the statistical uncertainty.

5. Weak lensing tomography

In this section we present our analysis of the redshift dependence of the lensing signal in COSMOS. We start with the definition of redshift bins in Sect. 5.1, summarize the theoretical framework in Sect. 5.2, describe our angular binning and treatment of intrinsic galaxy alignments in Sect. 5.3, elaborate on the covariance estimation in Sect. 5.4, present the measured redshift
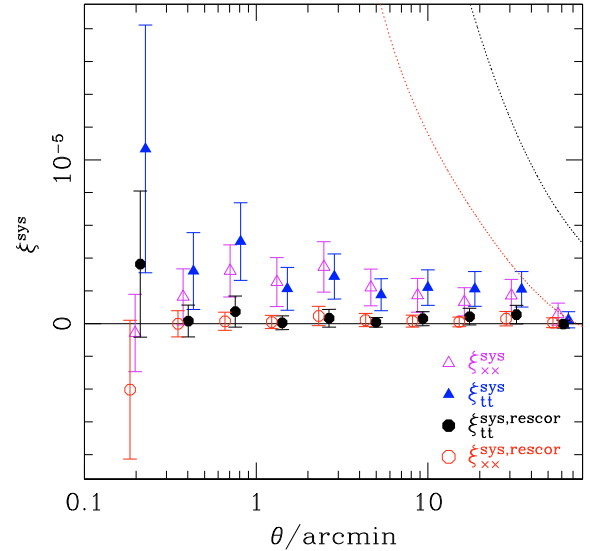

Fig. 5. Cross-correlation between galaxy shear estimates and uncorrected stellar ellipticities as defined in (12). The signal is consistent with zero if the residual ellipticity correction discussed in Appendix B.6 is applied (circles). Even without this correction (triangles) it is at a level negligible compared to the expected cosmological signal (dotted curves), except for the largest scales, where the error-budget is anyway dominated by sampling variance.

scaling in Sect. 5.5, and discuss indications for a contamination of faint $z_{\mathrm{phot}} < 0.6$ galaxies with high redshift galaxies in Sect. 5.6.

5.1. Redshift binning

We split the galaxies with individual COSMOS-30 photo-zs into five redshift bins, as summarized in Table 1 and illustrated in Fig. 6. We chose the intermediate limits $z = (0.6, 1.0, 1.3)$ such that the Balmer/4000 Å break is approximately located at the centre of one of the broadband $r^+ i^+ z^+$ filters. This minimizes the impact of possible artifical clustering in photo-z space and hence scatter between redshift bins for galaxies too faint to be detected in the Subaru medium bands. Given our chosen limits,

Table 1. Definition of redshift bins, number of contributing galaxies, and mean redshifts.

Bin	z_{min}	z_{max}	N	$\langle z \rangle$
1	0.0	0.6	$i^+ < 24 : 22\,294^a$	0.37
			$i^+ > 24 : 29\,817$	
2	0.6	1.0	58\,194	0.80
3	1.0	1.3	36\,382	1.16
4	1.3	2.0	25\,928	1.60
5	2.0	4.0	21\,718	2.61
6	0.0	5.0	251\,958	1.54 ± 0.15

Notes. $^{(a)}$ Here we also exclude 259 galaxies with $i^+ < 24$, which have a significant secondary peak in their redshift probability distribution at $z_{phot,2} > 0.6$.
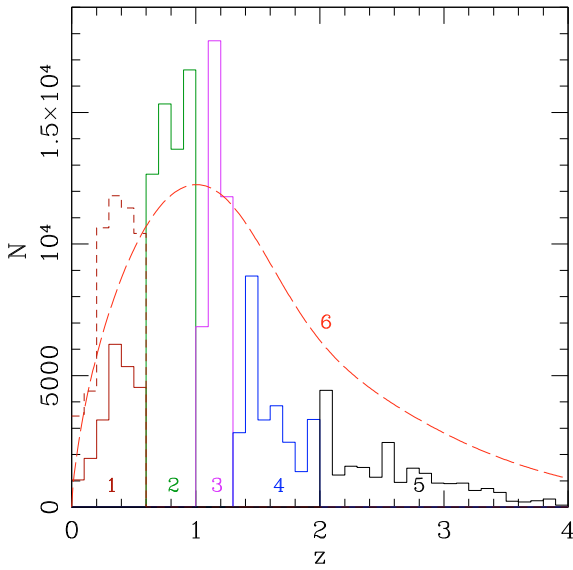
Fig. 6. Redshift distributions for our tomography analysis. The solid-line histogram shows the individual COSMOS-30 redshifts used for bins 1 to 5, while the difference between the dashed and solid histograms indicates the $24 < i^+ < 25$ galaxies with $z_{phot} < 0.6$, which are excluded in our analysis due to potential contamination with high-redshift galaxies. The long-dashed curve corresponds to the estimated redshift distribution for $i_{814} < 26.7$ shear galaxies without individual COSMOS-30 photo-z, which we use as bin 6.

most catastrophic redshift errors are faint bin 5 galaxies identified as bin 1 (Sect. 2.2.1). Thus, we do not include $z < 0.6$ galaxies with $i^+ > 24$ in our analysis due to their potential contamination with high redshift galaxies, but study their lensing signal separately in Sect. 5.6. We use all galaxies without individual photo-z estimates with $22 < i_{814} < 26.7$[7] as a broad bin 6, for which we estimated the redshift distribution in Sect. 2.2.2.

5.2. Theoretical description

Extending the formalism from Sect. 4, we split the galaxy sample into redshift bins and cross-correlate shear estimates between bins k and l

$$\hat{\xi}_{\pm}^{kl}(\theta) = \frac{\sum_{i,j} \left(\gamma_{t,i}^k \gamma_{t,j}^l \pm \gamma_{\times,i}^k \gamma_{\times,j}^l \right) \Delta_{ij}}{\sum_{i,j} \Delta_{ij}}, \tag{13}$$

---

[7] Including galaxies with $i^+ < 25$ which are located in masked regions for the ground-based photo-z catalogue, but not for the space-based lensing catalogue.

where the summation extends over all galaxies i in bin k, and all galaxies j in bin l. These are estimates for the shear cross-correlation functions $\xi_{\pm}^{kl}$, which are filtered versions of the convergence cross-power spectra

$$\xi_{+/-}^{kl}(\theta) = \frac{1}{2\pi} \int_0^\infty d\ell\, \ell\, J_{0/4}(\ell\theta) P_\kappa^{kl}(\ell), \tag{14}$$

where J_n denotes the nth-order Bessel function of the first kind and ℓ is the modulus of the two-dimensional wave vector. These can be calculated from line-of-sight integrals over the three-dimensional (non-linear) power spectrum P_δ (see Sect. 6.2) as

$$P_\kappa^{kl}(\ell) = \frac{9H_0^4 \Omega_m^2}{4c^4} \int_0^{\chi_h} d\chi \frac{g_k(\chi)g_l(\chi)}{a^2(\chi)} P_\delta\left(\frac{\ell}{f_K(\chi)}, \chi\right), \tag{15}$$

with the Hubble parameter H_0, matter density Ω_m, scale factor a, comoving radial distance χ, comoving distance to the horizon χ_h, and comoving angular diameter distance $f_K(\chi)$. The geometric lens-efficiency factors

$$g_k(\chi) \equiv \int_\chi^{\chi_h} d\chi'\, p_k(\chi') \frac{f_K(\chi' - \chi)}{f_K(\chi')} \tag{16}$$

are weighted according to the redshift distributions p_k of the two considered redshift bins (see e.g. Kaiser 1992; Bartelmann & Schneider 2001; Simon et al. 2004).

5.3. Angular binning and treatment of intrinsic galaxy alignments

Our six redshift bins define a total of 21 combinations of redshift bin pairs (including auto-correlations). For each redshift bin pair (k, l), we compute the shear cross-correlations ξ_+^{kl} and ξ_-^{kl} in six logarithmic angular bins between $0\rlap{.}'2$ and $30'$. We include all of these angular and redshift bin combinations in the analysis of the weak lensing redshift scaling presented in this section, to keep it as general as possible. Yet, for the cosmological parameter estimation in Sect. 6, we carefully select the included bins to minimize potential bias by intrinsic galaxy alignments and uncertainties in theoretical model predictions.

In order to minimize potential contamination by intrinsic alignments of physically associated galaxies, we exclude the auto-correlations of the relatively narrow redshift bins 1 to 5. These contain the highest fraction of galaxy pairs at similar redshift, and hence carry the strongest potential contamination.

An additional contamination may originate from alignments between intrinsic galaxy shapes and their surrounding density field causing the gravitational shear (e.g. Hirata & Seljak 2004; Hirata et al. 2007). A complete removal of this effect requires more advanced analysis schemes (e.g. Joachimi & Schneider 2008), which we postpone to a future study. Yet, following the suggestion by Mandelbaum et al. (2006), we exclude luminous red galaxies (LRGs) in the computation of the shear-shear correlations used for the parameter estimation. This reduces potential contamination, given that LRGs were found to carry the strongest alignment signal (Mandelbaum et al. 2006, 2009; Hirata et al. 2007). We select these galaxies from the Ilbert et al. (2009) photo-z catalogue with cuts in the photometric type $mod_{gal} \le 8$ ("ellipticals") and absolute magnitude $M_V < -19$, excluding a total of 5751 galaxies[8]. We accordingly adapt the redshift distribution for the parameter estimation.

---

[8] In the cross-correlation between two redshift bins, it would be sufficient to exclude LRGs in the lower redshift bin only. However, for convenience we generally exclude them.

In the cosmological parameter estimation, we additionally exclude the smallest angular bin ($\theta < 0\!.\!'5$), for which the theoretical model predictions have the largest uncertainty due to required non-linear corrections (Sect. 6.2) and the influence of baryons (e.g. Rudd et al. 2008).

While we do not exclude LRGs and the smallest angular bin for the redshift scaling analysis presented in the current section, we have verified that their exclusion leads to only very small changes, which are well within the statistical errors and do not affect our conclusions.

5.4. Covariance estimation

In order to interpret our measurement and constrain cosmological parameters, we need to reliably estimate the data covariance matrix and its inverse. Massey et al. (2007c) estimate a covariance for their analysis from the variation between the four COSMOS quadrants. This approach yields too few independent realizations and may substantially underestimate the true errors (Hartlap et al. 2007). We also do not employ a covariance for Gaussian statistics (e.g. Joachimi et al. 2008) due to the neglected influence of non-Gaussian sampling variance. This is particularly important for the small-scale signal probed with COSMOS (Kilbinger & Schneider 2005; Semboloni et al. 2007). Instead, we estimate the covariance matrix from 288 realizations of COSMOS-like fields obtained from ray-tracing through the Millennium Simulation (Springel et al. 2005), which combines a large simulated volume yielding many quasi-independent lines-of-sight with a relatively high spatial and mass resolution. The latter is needed to fully utilize the small-scale signal measurable in a deep space-based survey.

The details of the ray-tracing analysis are given in Hilbert et al. (2009). In brief, we use tilted lines-of-sight through the simulation to avoid repetition of structures along the backwards lightcone, providing us with 32 quasi-independent 4 deg×4 deg fields, which we further subdivide into nine COSMOS-like subfields, yielding a total of 288 realizations. We randomly populate the fields with galaxies, employing the same galaxy number density, field masks, shape noise, and redshift distribution as in the COSMOS data. We incorporate photometric redshift errors for bins 1 to 5 by randomly misplacing galaxy redshifts assuming a (symmetric) Gaussian scatter according to the 1σ errors in the photo-z catalogue. In contrast, the redshift calibration uncertainty for bin 6 is not a stochastic but a systematic error, which we account for in the cosmological model fitting in Sect. 6.

The value of $\sigma_8 = 0.9$ used for the Millennium Simulation is slightly high compared to current estimates. This will lead to an overestimation of the errors, hence our analysis can be considered slightly conservative. We have to neglect the cosmology dependence of the covariance (Eifler et al. 2009) in the parameter estimation, given that we have currently only one simulation with high resolution and large volume at hand.

We need to invert the covariance matrix for the cosmological parameter estimation in Sect. 6. While the covariance estimate $\hat{C}_*$ from the ray-tracing realizations is unbiased, a bias is introduced by correlated noise in the matrix inversion. To obtain an unbiased estimate for the inverse covariance C^{-1}, we apply the correction

$$\hat{C}^{-1} = c\,\hat{C}_*^{-1} = \frac{n - p - 2}{n - 1}\hat{C}_*^{-1} \quad \text{for } p < n - 2 \qquad (17)$$

discussed in Hartlap et al. (2007), where $n = 288$ is the number of independent realizations and p is the dimension of the data
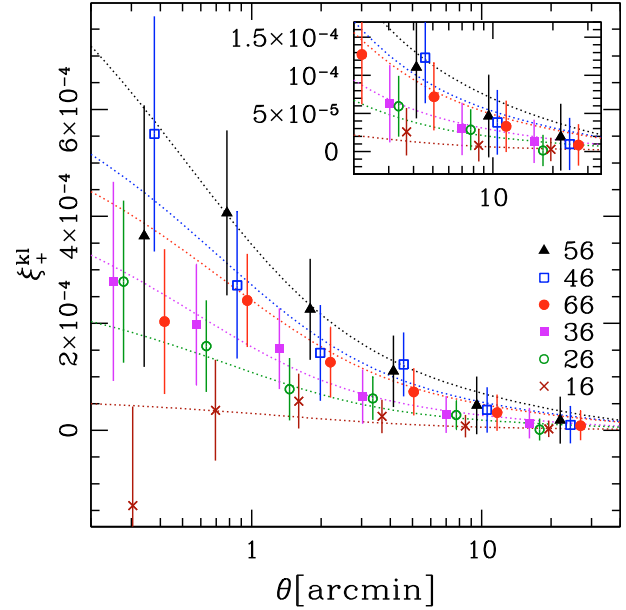

Fig. 7. Shear-shear cross-correlations ξ_+^{k6} between bins 1 to 6 and bin 6, where points are plotted at their *effective* θ, weighted within one bin according to the θ-dependent number of contributing galaxy pairs. The curves indicate ΛCDM predictions for our reference cosmology with $\sigma_8 = 0.8$. Corresponding points and curves have been equally offset along the x-axis for clarity. The error-bars correspond to the square root of the diagonal elements of the full ray-tracing covariance. Note that the points are substantially correlated both between angular and redshift bins, leading to the smaller scatter than naively expected from the error-bars.

vector. As discussed in Sect. 5.3, we exclude the smallest angular bin and auto-correlations of redshift bins 1 to 5, yielding $p = 160$ and a moderate correction factor $c \simeq 0.4390$. In contrast, for the full data vector including all bins and correlations ($p = 252$), a very substantial correction factor $c \simeq 0.1185$ would be required. Thus, our optimized data vector also leads to a more robust covariance inversion.

In order to limit the required correction for the covariance inversion, we do not include more angular bins in our analysis. We have therefore optimized the bin limits using Gaussian covariances (Joachimi et al. 2008) and a Fisher-matrix analysis aiming at maximal sensitivity to cosmological parameters.

5.5. Redshift scaling of shear-shear cross-correlations

We plot the shear-shear cross-correlations ξ_+^{k6} between all redshift bins and the broad bin 6 in Fig. 7. These cross-correlations carry the lowest shot noise and shape noise due to the large number of galaxies in bin 6. The good agreement between the data and ΛCDM model already indicates that the weak lensing signal roughly scales with redshift as expected. The errors correspond to the square root of the diagonal elements of the full ray-tracing covariance. Points are correlated not only within a redshift bin pair, but also between different redshift combinations, as their lensing signal is partially caused by the same foreground structures. In addition, galaxies in bin 6 contribute to different cross-correlations. Note that our relatively broad angular bins lead to a significant variation of the theoretical models *within* a bin. When computing an average model prediction for a bin, we therefore weight according to the θ-dependent number of galaxy pairs within this bin. Likewise, we plot points at their *effective* θ, which has been weighted accordingly.
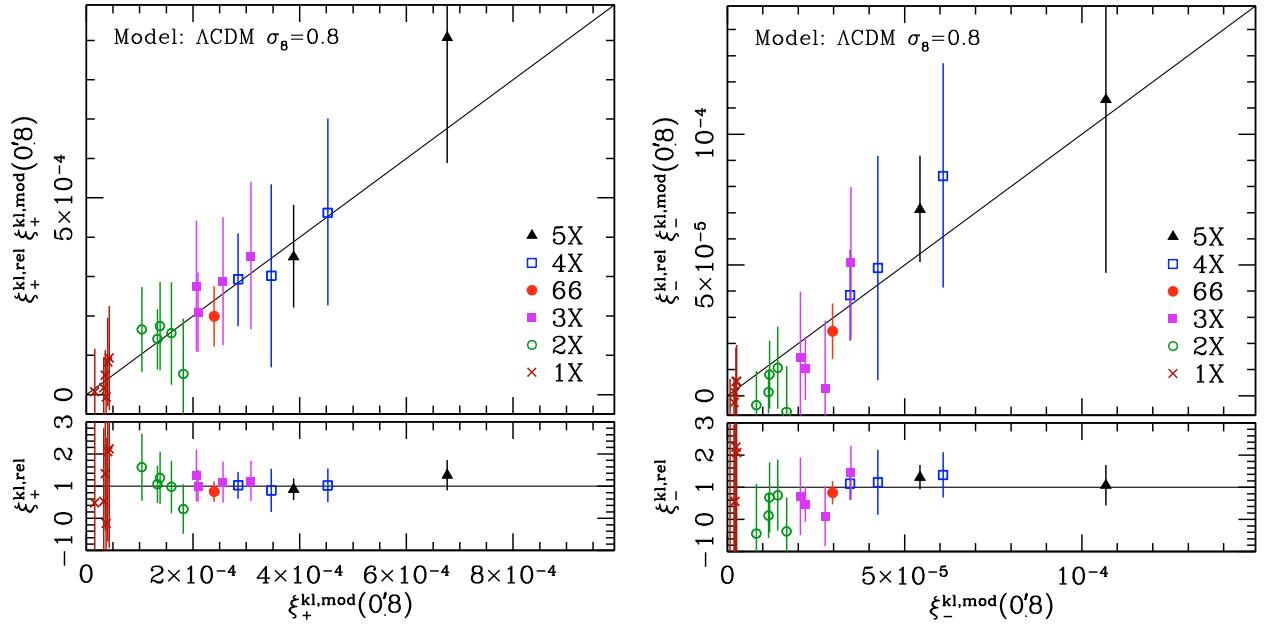
Fig. 8. Shear-shear redshift scaling for ξ_+ (*left*) and ξ_- (*right*). Each point corresponds to one redshift bin combination, where we have combined different angular scales by fitting the signal amplitude $\xi_{\pm}^{kl,\text{rel}}$ relative to the model prediction $\xi_{\pm}^{kl,\text{mod}}(\theta)$ for our reference ΛCDM cosmology with $\sigma_8 = 0.8$. The *lower* plots show the relative amplitude as a function of the model prediction $\xi_{\pm}^{kl,\text{mod}}(0.8)$ for a reference angular bin centred at $\theta = 0.8$, whereas the amplitude has been scaled with $\xi_{\pm}^{kl,\text{mod}}(0.8)$ for the *upper* plots. Symbols of one kind correspond to cross-correlations of one bin with all higher-numbered bins. Within one symbol the partner redshift bins sort according to the mean lensing efficiency, from left to right as 1, 2, 3, 6, 4, 5. Note that points are correlated as each redshift bin is used for six bin combinations, and given that foreground structures contribute to the signal of all bin combinations at higher redshift. The error-bars are computed from the full ray-tracing covariance, accounting for this influence of large-scale structure.

Instead of plotting 21 separation-dependent, noisy cross-correlations, we condense the information into a single plot showing the redshift dependence of the signal. Here we assume that the predictions for our reference cosmology describe the relative *angular* dependence of the signal sufficiently well, and fit the data points as

$$\xi_{\pm}^{kl,\text{fit}}(\theta) = \xi_{\pm}^{kl,\text{rel}} \xi_{\pm}^{kl,\text{mod}}(\theta), \tag{18}$$

where $\xi_{\pm}^{kl,\text{mod}}(\theta)$ is the model for the reference cosmology with $\sigma_8 = 0.8$, and $\xi_{\pm}^{kl,\text{rel}}$ is the fitted relative amplitude. In this fit, we take the full ray-tracing covariance between the angular scales into account. We plot the resulting 21 "collapsed" cross-correlations for both ξ_+ and ξ_- in Fig. 8, as a function of their model prediction at a reference angular scale of 0.8, where points are again correlated. For both cases the redshift scaling of the signal is fully consistent with ΛCDM expectations, showing a strong increase with redshift. This demonstrates that 3D weak lensing does indeed perform as expected. We note that for ξ_- the signal is somewhat low for lower redshift combinations (smaller $\xi_{\pm}^{kl,\text{mod}}$), whereas it is slightly increased compared to predictions at higher redshifts. This behaviour is not surprising as most massive structures in COSMOS are located at $0.7 \lesssim z \lesssim 0.9$ (Scoville et al. 2007b), which create a lensing signal only for the higher redshift source bins. Slight differences between ξ_+ and ξ_- are also expected, given that they probe the power spectrum with different filter functions, see Eq. (14).

5.6. Contamination of the excluded faint $z < 0.6$ sample with high-z galaxies

As discussed in Sect. 2.2, we expect a significant fraction of faint $i^+ \gtrsim 24$ galaxies with assigned photometric redshift $z_{\text{phot}} < 0.6$

to be truly located at high redshifts $z_{\text{true}} \gtrsim 2$. To test this hypothesis, we plot the collapsed shear cross-correlations for different samples of galaxies with assigned $z_{\text{phot}} < 0.6$ in Fig. 9. For the $i^+ < 24$ galaxies used in the cosmological analysis the signal is well consistent with expectations, suggesting negligible contamination. For a $24 < i^+ < 25$ sample with single-peaked photo-z probability distribution a mild increase is detected. This is still consistent with expectations, suggesting at most low contamination. We also study a sample of galaxies each of which has a significant secondary peak in their photometric redshift probability distribution at $z_{\text{phot},2} > 0.6$, amounting to 36% of all $24 < i^+ < 25$ galaxies with $z_{\text{phot}} < 0.6$. This sample shows a strong boost in the lensing signal, suggesting strong contamination with high-redshift galaxies.

We can obtain a rough estimate for this contamination if we assume that the shear signal does actually scale as in our reference ΛCDM cosmology. For simplicity we assume that the cross-contamination can be described as a uni-directional scatter from bin 5 to bin 1, and that the true redshifts of the misplaced galaxies follow the distribution within bin 5. The expected contaminated signal is then given as a linear superposition of the cross-correlation predictions with bin 1 and bin 5 respectively, according to the relative number of contributing galaxy pairs

$$\xi_+^{11,\text{cont}} = (1-r)^2 \xi_+^{11,\text{mod}} + r^2 \xi_+^{55,\text{mod}} + 2r(1-r)\xi_+^{15,\text{mod}} \tag{19}$$

$$\xi_+^{1l,\text{cont}} = (1-r)\xi_+^{1l,\text{mod}} + r\xi_+^{l5,\text{mod}}, \quad \text{for } l > 1,$$

where r is the contamination fraction, i.e. the fraction of the bin 1 galaxies with $24 < i^+ < 25$ and a significant secondary peak in their photo-z PDF, which should have been placed into bin 5. We fit the measured shear-shear cross-correlations ξ_+^{1l} with (19) as a function of r, where we fix the reference ΛCDM cosmology and employ a special ray-tracing covariance
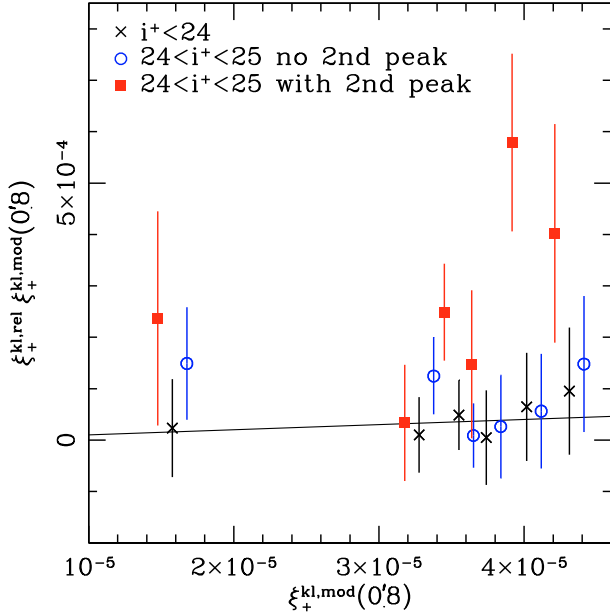
Fig. 9. Shear-shear redshift scaling for ξ_+^{1l} as in Fig. 8, but now only cross-correlations with bin 1 ($z < 0.6$) are shown, hence the different axis scale. The signal from the $i^+ < 24$ galaxies used in our cosmological analysis (crosses), is well consistent with the ΛCDM prediction (curve). Galaxies with $24 < i^+ < 25$ and a single-peaked photo-z probability distribution (circles) show a mildly increased but still consistent signal. In contrast, $24 < i^+ < 25$ galaxies with a significant secondary peak at $z_{phot,2} > 0.6$ in their individual photo-z probability distribution, show a strong signal excess (squares), suggesting strong contamination with high-redshift galaxies.

(generated for $r = 0.5$), yielding an estimate for the contamination $r = 0.7 \pm 0.2$ (stat.) ± 0.1 (sys.), where the systematic error indicates the response to a change in σ_8 by 0.1. This translates to a total contamination of $(25 \pm 7 \pm 4)\%$ for the $24 < i^+ < 25$ galaxies with $z_{phot} < 0.6$, which is consistent with our estimate for the redshift calibration uncertainty for bin 6 (Sect. 2.2.2). Note that we also measure an increased signal in ξ_-^{1l} for the sample with secondary photometric redshift peak, but do not include it in the fit (19) due to the stronger deviations for $\xi_-^{kl,rel}$ in Fig. 8. An adequate inclusion would then require a more complex analysis scheme, with a comparison not to the model predictions, but to all measured cross-correlations.

Our analysis provides an interesting confirmation for the photometric redshift analysis by Ilbert et al. (2009), which apparently succeeds in identifying sub-samples of (mostly) uncontaminated and potentially contaminated galaxies quite efficiently.

6. Constraints on cosmological parameters

6.1. Parameter estimation and considered cosmological models

The statistical analysis of the shear tomography correlation functions, assembled as data vector d, is based on a standard Bayesian approach (e.g. MacKay 2003). Therein, prior knowledge of model parameters p is combined with the information on those parameters inferred from the new observation and expressed as posterior probability distribution function (PDF) of p:

$$P(p|d) = \frac{P(d|p)P(p)}{P(d)}. \tag{20}$$

Here, $P(p)$ is the prior based on theoretical constraints and previous observations, and $P(d)$ denotes the evidence. The likelihood function $P(d|p)$ is the statistical model of the measurement noise, for which we choose a Gaussian model

$$\ln P(d|p) = -\frac{1}{2}[d - m(p)]^t C^{-1}[d - m(p)] + \text{const}, \tag{21}$$

where $m(p)$ is the parameter-dependent model, and C^{-1} the inverse covariance, which we estimated from the ray-tracing realizations in Sect. 5.4.

In our analysis we consider different cosmological models, which are characterized by the parameters $p = (\Omega_{DE}, \Omega_m, \sigma_8, h, w, f_z)$, with the dark energy density Ω_{DE}, matter density Ω_m, power spectrum normalization σ_8, Hubble parameter h, and (constant) dark energy equation of state parameter w. Here, f_z denotes a nuisance parameter encapsulating the uncertainty in the redshift calibration for bin 6 as $p_6(z, f_z) \equiv p_6(f_z z)$, which was discussed in Sect. 2.2.2. We consider

- a **flat ΛCDM** cosmology with fixed $w = -1$, $\Omega_m \in [0, 1]$, and $\Omega_{DE} = \Omega_\Lambda = 1 - \Omega_m$,
- a **general (non-flat) ΛCDM** cosmology with fixed $w = -1$ and $\Omega_{DE} = \Omega_\Lambda \in [0, 2]$, $\Omega_m \in [0, 1.6]$, and
- a **flat wCDM** cosmology with $w \in [-2, 0]$, $\Omega_m \in [0, 1]$, and $\Omega_{DE} = 1 - \Omega_m$.

In all cases, we employ priors with flat PDFs for $\sigma_8 \in [0.2, 1.5]$ and $f_z \in [0.9, 1.1]$.

In our default analysis scheme we also apply a Gaussian prior for $h = 0.72 \pm 0.025$, and assume a fixed baryon density $\Omega_b = 0.044$ and spectral index $n_s = 0.96$ as consistent with Dunkley et al. (2009), where the small uncertainties on Ω_b and n_s are negligible for our analysis. Note that we relax these priors for parts of the analysis in Sects. 6.3.2 and 6.4.

The practical challenge of the parameter estimation is to evaluate the posterior within a reasonable time, as the computation of one model vector for shear tomography correlations is time-intensive. For an efficient sampling of the parameter space, we employ the Population Monte Carlo (PMC) method as described in Wraith et al. (2009). This algorithm is an adaptive importance-sampling technique (Cappé et al. 2008): instead of creating a sample under the posterior as done in traditional Monte-Carlo Markov chain (MCMC) techniques (e.g. Christensen et al. 2001), points are sampled from a simple distribution, the so-called proposal, in our case a mixture of eight Gaussians. Each point is then weighted by the ratio of the proposal to the posterior at that point. In a number of iterative steps, the proposal function is adapted to give better and better approximations to the posterior. We run the PMC algorithm for up to eight iterations, using 5000 sample points in each iteration. To reduce the Monte-Carlo variance, we use larger samples with 10 000 to 20 000 points for the final iteration. These are used to create density histograms, mean parameter values, and confidence regions. Depending on the experiment, the effective sample size of the final importance sample was between 7500 and 17 700. We also cross-checked parts of the analysis with an independently developed code which is based on the traditional but less efficient MCMC approach, finding fully consistent results.

6.2. Non-linear power spectrum corrections

To calculate model predictions for the correlation functions according to (14), (15), and (16), we need to evaluate the involved
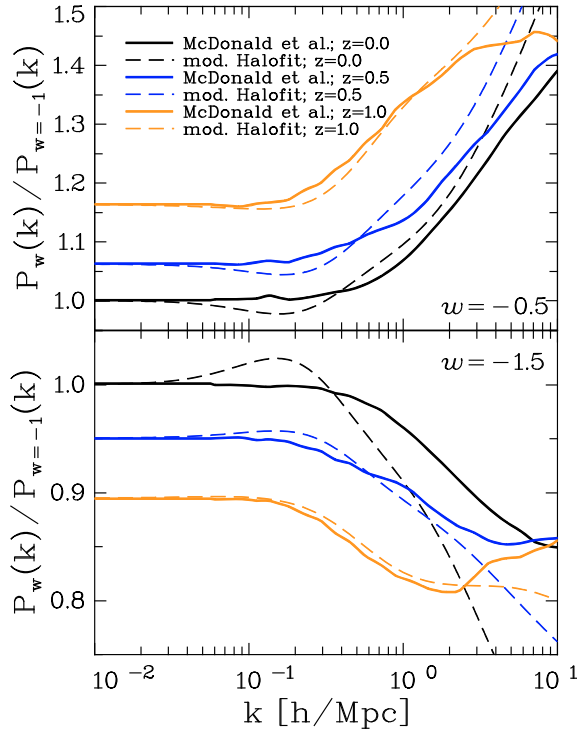
Fig. 10. Comparison of the fit formulae for the non-linear growth of structure in wCDM cosmologies. Shown is the three-dimensional matter power spectrum, normalized by the corresponding ΛCDM power spectrum, as a function of the wave vector k. In the *upper panel* we consider a wCDM cosmology with $w = -0.5$, in the *lower panel* one with $w = -1.5$. Solid curves show the fit to the simulations by McDonald et al. (2006), while the dashed lines have been obtained by interpolating the Smith et al. (2003) fitting formulae between the cases of an OCDM and a ΛCDM cosmology as outlined in Sect. 6.2. Each fit formula has been computed at redshifts $z = 0$ (black), $z = 0.5$ (blue), and $z = 1$ (orange). While deviations are substantial at $z = 0$, the lensing analysis of the deep COSMOS data is mostly sensitive to structures at $z \gtrsim 0.4$, where deviations are reasonably small. Note that the remaining cosmological parameters have been set to their default WMAP5-like values, except for $\sigma_8 = 0.9$.

distance ratios and compute the non-linear power spectrum $P_\delta(k, z)$. Given a set of parameter values, the computation of the distances and the linearly extrapolated power spectrum is straightforward. We employ the transfer function by Eisenstein & Hu (1998) for the latter, taking baryon damping but no oscillations into account ("shape fit").

For ΛCDM models we estimate the full non-linear power spectrum according to Smith et al. (2003). McDonald et al. (2006) also provide non-linear power spectrum corrections for $w \neq -1$, but these were tested for a narrow range in $\sigma_8 = 0.897 \pm 0.097$ only. We want to keep our analysis as general as possible, not having to assume such a strong prior on σ_8. Following the icosmo code (Refregier et al. 2008) we instead interpolate the non-linear corrections from Smith et al. (2003) between the cases of a ΛCDM cosmology ($w = -1$) and an OCDM cosmology, acting as a dark energy with $w = -1/3$. This is achieved by replacing the parameter $f = \Omega_\Lambda / (1 - \Omega_m)$ in the halo model fitting function (Smith et al. 2003). This parameter is used to interpolate between spatially flat models with dark energy ($f = 1$) and an open Universe without dark energy ($f = 0$). We substitute f by a new parameter $f' \equiv -0.5(3w + 1)$. Thus, we obtain $f' = 1$ for ΛCDM and $f' = 0$ for wCDM
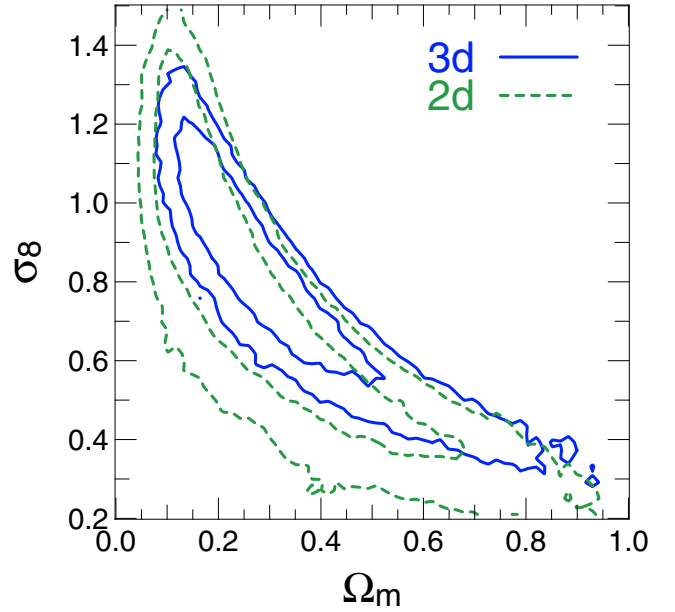
Fig. 11. Comparison of our constraints on Ω_m and σ_8 for a flat ΛCDM cosmology using a 3D (blue solid contours) versus a 2D weak lensing analysis (green dashed contours). The contours show the 68.3% and 95.4% credibility regions, where we have marginalized over the parameters which are not shown. The 2D analysis favours slightly lower σ_8 resulting from the lack of massive structures in the field at low redshifts. Nonetheless, the constraints are fully consistent as our ray-tracing covariance properly accounts for sampling variance.

with $w = -1/3$, mimicking an OCDM cosmology for which the original parameter f vanished as well.

To test this simplistic approximation, we compare the computed corrections for $w = (-0.5, -1.5)$ to the fitting formulae from McDonald et al. (2006) in Fig. 10. Note that we use our fiducial cosmological parameters to obtain these curves, except for $\sigma_8 = 0.9$, to match $\sigma_8 = 0.897 \pm 0.097$ from McDonald et al. (2006). For most of the scales probed by our measurement the two descriptions agree reasonably well. The modification of the halo fit follows the fits to the simulations more accurately on large scales and at higher redshift, while it does not reproduce the tendency of the fits by McDonald et al. (2006) to drop off for large wave vectors. The precision of the modification outlined above is sufficient for our aim to provide a proof of concept for weak lensing dark energy measurements. However, future measurements with larger data sets will require accurate fitting formulae for general w cosmologies.

6.3. Cosmological constraints from COSMOS

6.3.1. Flat ΛCDM cosmology

We plot our constraints on Ω_m and σ_8 for a flat ΛCDM cosmology and our default 3D lensing analysis scheme in Fig. 11 (solid contours), showing the typical "banana-shaped" degeneracy, from which we compute[9]

$$\sigma_8 (\Omega_m / 0.3)^{0.51} = 0.79 \pm 0.09 \quad (68.3\% \text{ conf.}).$$

Here we marginalize over the uncertainties in h and the parameter f_z encapsulating the uncertainty in the redshift calibration for bin 6, where we find that f_z is nearly uncorrelated

---

[9] Here, we fit a power-law with slope α minimizing the separation to all posterior-weighted points in the $\Omega_m - \sigma_8$ plane, and compute the 1D marginalized mean of $\sigma_8 (\Omega_m / 0.3)^\alpha$ within $\Omega_m \in [0.275, 0.325]$.

Table 2. Constraints on $\sigma_8 \, (\Omega_m/0.3)^\alpha$, Ω_m, Ω_{DE}, and w from the COSMOS data for different cosmological models and analysis schemes.

Cosmology	Analysis	α	$\sigma_8 \, (\Omega_m/0.3)^\alpha$	Ω_m	Ω_{DE}	w
Flat ΛCDM	3D	0.51	0.79 ± 0.09	$0.32^{+0.34}_{-0.11}$	$0.68^{+0.11}_{-0.34}$	-1
Flat ΛCDM	2D	0.62	0.68 ± 0.11	$0.30^{+0.44}_{-0.15}$	$0.70^{+0.15}_{-0.44}$	-1
General ΛCDM	3D	0.77	0.74 ± 0.12	$0.43^{+0.40}_{-0.19}$	$0.97^{+0.39}_{-0.60}$	-1
Flat wCDM	3D	0.47	0.79 ± 0.09	$0.30^{+0.39}_{-0.11}$	$0.70^{+0.11}_{-0.39}$	$-1.23^{+0.79}_{-0.50}$

Notes. Here we use our default priors and quote the marginalized mean and 68.3% confidence limits (16th and 84th percentiles) assuming non-linear power spectrum corrections according to Smith et al. (2003) and the description given in Sect. 6.2. Our analysis of the Millennium Simulation (Sect. 6.4) suggests that the σ_8-estimates should be reduced by a factor $\times 0.95$ due to biased model predictions for the non-linear power spectrum and reduced shear corrections. The power-law slopes α have typical fit uncertainties of $\sigma_\alpha \simeq 0.02$.

with Ω_m, and only weakly correlated with σ_8. The data allow us to weakly constrain $f_z = 1.03^{+0.06}_{-0.04}$, with a maximum posterior point at $f_z = 1.05$. This constraint is nearly unchanged for the other cosmological models considered below.

For comparison we also conduct a classic 2D lensing analysis (dashed contours in Fig. 11), where we use only the total redshift distribution and do not split galaxies into redshift bins. We find that the 2D and 3D analyses yield consistent results with substantially overlapping 1σ regions, as expected. Yet, the constraints from the 2D analysis shift towards lower $\sigma_8 \, (\Omega_m/0.3)^{0.62} = 0.68 \pm 0.11$. The difference is not surprising given that the strongest contribution to the lensing signal in COSMOS comes from massive structures near $z \sim 0.7$ (Scoville et al. 2007b; Massey et al. 2007b), boosting the signal for high redshift sources, but leading to a lower signal for galaxies at low and intermediate redshifts (see right panel of Fig. 8). The 3D lensing analysis can properly combine these measurements, also accounting for the stronger impact of sampling variance at low redshifts. In contrast, the 2D lensing analysis leads to a rather low (but still consistent) estimate for σ_8, due to the large number of low and intermediate redshift galaxies with low shear signal.

The tomographic analysis also reduces the degeneracy between Ω_m and σ_8 by probing the redshift-dependent growth of structure and distance-redshift relation, which differ substantially for a concordance ΛCDM cosmology and e.g. an Einstein-de Sitter cosmology ($\Omega_m = 1$). We summarize our parameter estimates in Table 2, also for the other cosmological models considered in the following subsections.

We also test our selection criteria for the optimized data vector (Sect. 5.3) by analysing several deviations from it for a flat ΛCDM cosmology. We find negligible influence if the smallest angular scales $\theta < 0\rlap{.}'5$ or LRGs are included, suggesting that the measurement is robust regarding the influence of small-scale modelling uncertainties and intrinsic alignments between galaxy shapes and their surrounding density field. Performing the analysis using *only* the usually excluded auto-correlations of the relatively narrow redshift bins 1 to 5, we measure a slightly lower $\sigma_8 \, (\Omega_m/0.3)^{0.52} = 0.70 \pm 0.13$, which is still consistent given the substantially degraded statistical accuracy. If intrinsic alignments between physically associated galaxies contaminate the lensing measurement, we expect these auto-correlations to be most strongly affected. However, models predict an excess signal (e.g. Heymans et al. 2006b), whereas we measure a slight decrease within the statistical errors. Thus, we detect no significant indication for contamination by intrinsic galaxy alignments.

6.3.2. General (non-flat) ΛCDM cosmology

We plot our constraints for a general ΛCDM cosmology without the assumption of flatness in Fig. 12. From the lensing data we find

$$\Omega_\Lambda > 0.32 \quad (90\% \, \text{conf.}),$$

where our prior excludes negative densities $\Omega_\Lambda < 0$. Based on our $\Omega_m - \Omega_\Lambda$ constraints, we compute the posterior PDF for the deceleration parameter

$$q_0 = -\ddot{a}a/\dot{a}^2 = \Omega_m/2 - \Omega_\Lambda \qquad (22)$$

as shown in Fig. 13, which yields

$$q_0 < 0 \quad (96.0\% \, \text{conf.}).$$

Relaxing our priors to $h = 0.72 \pm 0.08$ (HST Key Project, Freedman et al. 2001), $\Omega_b h^2 = 0.021 \pm 0.001$ (Big-Bang nucleosynthesis, Iocco et al. 2009), and $n_s \in [0.7, 1.2]$, weakens this constraint only slightly to

$$q_0 < 0 \quad (94.3\% \, \text{conf., weak priors}).$$

Employing the recent distance ladder estimate $h = 0.742 \pm 0.036$ (Riess et al. 2009) instead of the HST Key Project constraint, we obtain $q_0 < 0$ at 94.8% confidence.

Our analysis provides evidence of the accelerated expansion of the Universe ($q_0 < 0$) from weak gravitational lensing. While the statistical accuracy is still relatively weak due to the limited size of the COSMOS field, this evidence is independent of external constraints on Ω_m and Ω_Λ.

We note that the lensing data alone cannot formally exclude a non-flat OCDM cosmology. However, the cosmological parameters inferred for such a model would be inconsistent with various other cosmological probes[10]. We therefore perform our analysis in the context of the well-established ΛCDM model, where the lensing data provide additional evidence for cosmic acceleration.

---

[10] For a lensing-only OCDM analysis the posterior peaks at $\Omega_m \simeq 0.1$, $\sigma_8 \simeq 1.4$ (close to the prior boundaries). In the comparison with a ΛCDM analysis, the additional parameter Ω_Λ causes a penalty in the Bayesian model comparison (computed as in Kilbinger et al. 2009b). This leads to an only slightly larger evidence for the non-flat ΛCDM model compared to the OCDM model, with an inconclusive evidence ratio of 65:35. The evidence ratio becomes a "weak preference" (77:23) if we employ a (still conservative) prior $\sigma_8 < 1$. Thus, with this prior the ΛCDM model makes the data more than 3 times more probable than the OCDM model.
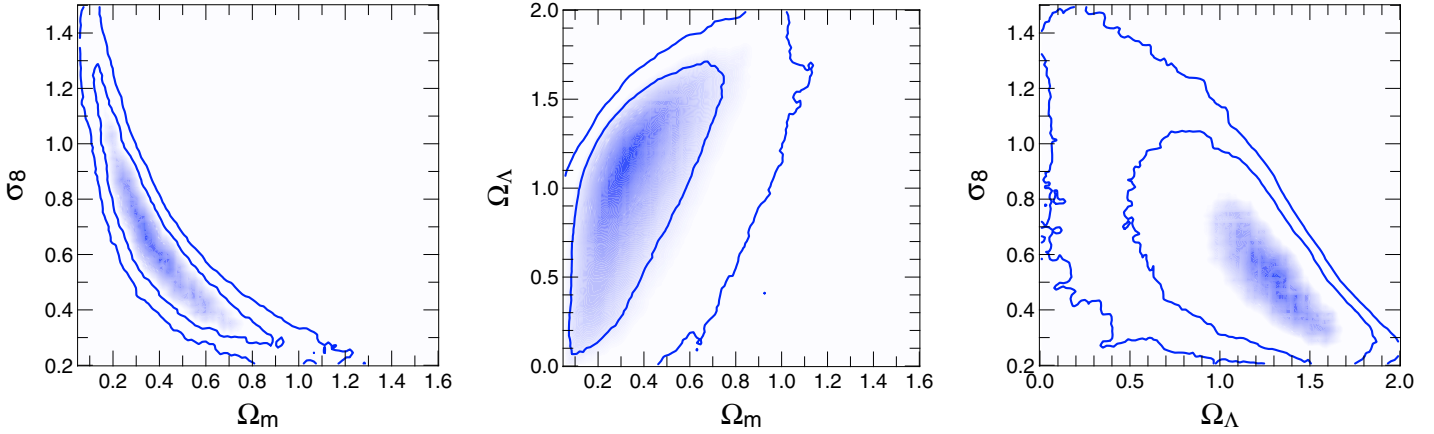
Fig. 12. Constraints on Ω_m, Ω_Λ, and σ_8 from our 3D weak lensing analysis of COSMOS for a general (non-flat) ΛCDM cosmology using our default priors. The contours indicate the 68.3% and 95.4% credibility regions, where we have marginalized over the parameters which are not shown. The non-linear blue-scale indicates the highest density region of the posterior.

6.3.3. Flat wCDM cosmology

For a flat wCDM cosmology we plot our constraints on the (constant) dark energy equation of state parameter w in Fig. 14, showing that the measurement is consistent with ΛCDM ($w = -1$). From the posterior PDF we compute

$$w < -0.41 \quad (90\% \,\text{conf.})$$

for the chosen prior $w \in [-2, 0]$. The exact value of this upper limit depends on the lower bound of the prior PDF given the non-closed credibility regions. We have chosen this prior as more negative w would require a worrisome extrapolation for the non-linear power spectrum corrections (Sect. 6.2). For comparison, we repeat the analysis with a much wider prior $w \in [-3.5, 0.5]$ leading to a stronger upper limit $w < -0.78$ (90% conf.). While the COSMOS data are capable to exclude very high values $w \gg -1$, larger lensing data sets will be required to obtain really competitive constraints on w.

To test the consistency of the data with ΛCDM, we compare the Bayesian evidence of the flat ΛCDM and wCDM models, which we compute in the PMC analysis as detailed in Kilbinger et al. (2009b). Here we find completely inconclusive probability ratios for wCDM versus ΛCDM of 52 : 48 ($w \in [-2, 0]$) and 45 : 55 ($w \in [-3.5, 0.5]$), confirming that the data are fully consistent with ΛCDM.

6.4. Model recalibration with the millennium simulation and joint constraints with WMAP-5

Heitmann et al. (2010) and Hilbert et al. (2009) found that the Smith et al. (2003) fitting functions slightly underestimate non-linear corrections to the power spectrum. To test whether this has a significant influence on our results, we performed a 3D cosmological parameter estimation using the mean data vector of the 288 COSMOS-like ray-tracing realizations from the Millennium Simulation. Here we modify the strong priors given in Sect. 6.1 to match the input values of the simulation ($\Omega_m = 0.25$, $\sigma_8 = 0.9$, $n_s = 1$, $h = 0.73$, $\Omega_b = 0.045$), and find $\sigma_8 = 0.947 \pm 0.006$[11] for $\Omega_m = 0.25$. This confirms the result

---

[11] Here we have scaled the uncertainty for the mean ray-tracing data vector from the uncertainty for a single COSMOS-like field assuming that all realizations are completely independent. This is slightly optimistic given the large but finite volume of the simulation, and fact that the realizations were cut from larger fields.
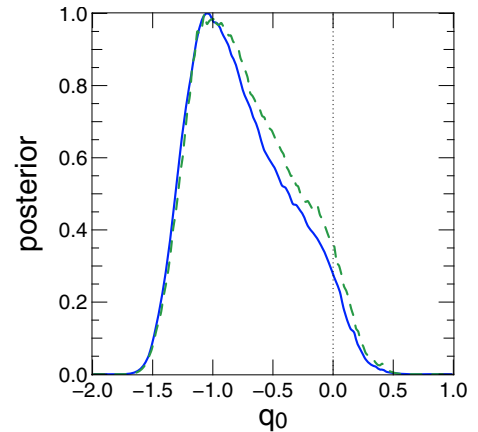
Fig. 13. Posterior PDF for the deceleration parameter q_0 as computed from our constraints on Ω_m and Ω_Λ for a general (non-flat) ΛCDM cosmology, using our default priors (solid curve), and using weaker priors from the HST Key Project and Big-Bang nucleosynthesis (dashed curve). The line at $q_0 = 0$ separates accelerating ($q_0 < 0$) and decelerating ($q_0 > 0$) cosmologies. We find $q_0 < 0$ at 96.0% confidence using our default priors, or 94.3% confidence for the weaker priors.
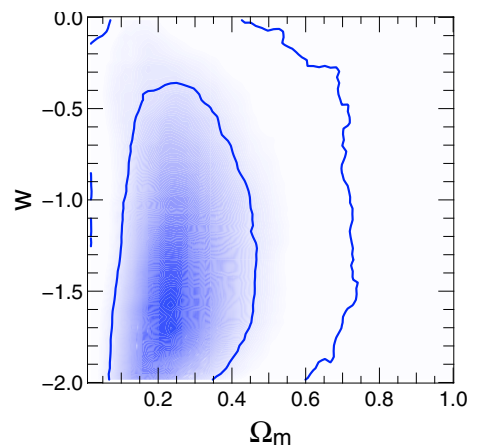

Fig. 14. Constraints on Ω_m and w from our 3D weak lensing analysis of COSMOS for a flat wCDM cosmology, assuming a prior $w \in [-2, 0]$. The contours indicate the 68.3% and 95.4% credibility regions, where we have marginalized over the parameters which are not shown. The non-linear blue-scale indicates the highest density region of the posterior.

of Heitmann et al. (2010) and Hilbert et al. (2009), indicating that models based on Smith et al. (2003) slightly underestimate the shear signal, hence a higher σ_8 is required to fit the data. Here we use actual *reduced shear* estimates from the simulation, but employ *shear* predictions, as done for the real data (see Sect. 4). Using *shear* estimates from the simulation yields $\sigma_8 = 0.936 \pm 0.006$. Thus, a minor contribution to the overestimation of σ_8 is caused by the negligence of reduced shear corrections (see also Dodelson et al. 2006; Shapiro 2009; Krause & Hirata 2009).

To compensate for this underestimation of the model predictions and reduced shear effects, we scale our derived constraints on σ_8 for a flat ΛCDM cosmology by a factor $0.9/0.947 \simeq 0.950$[12], yielding

$$\sigma_8 \, (\Omega_\mathrm{m}/0.3)^{0.51} = 0.75 \pm 0.08 \quad \text{(68.3\% conf., MS-calib.)}.$$

Note that we did not apply this correction for the values given in the previous section and listed in Table 2, as we can only test it for the case of a flat ΛCDM cosmology. Additionally, we want to keep the results comparable to previous weak lensing studies, which we expect to be similarly affected.

Having eliminated this last source of systematic uncertainty, we now estimate joint constraints with WMAP-5 CMB-only data (Dunkley et al. 2009), conducted similarly to the analysis by Kilbinger et al. (2009a). Here we assume a flat ΛCDM cosmology, completely relax our priors to $\Omega_\mathrm{b} \in [0.01, 0.1]$, $n_\mathrm{s} \in [0.7, 1.2]$, $h \in [0.2, 1.4]$, and scale σ_8 for the lensing model calculation according to the Millennium Simulation results. Here we also marginalize over an additional 2% uncertainty in the lensing σ_8 calibration to account for the dropped remaining mean shear calibration bias (0.8%, Sect. 3) and limited accuracy of the employed residual shear correction (Sect. 4), which we estimate to be 1% in σ_8. From the joint analysis with WMAP-5 we find

$$\Omega_\mathrm{m} = 0.266^{+0.025+0.057}_{-0.023-0.042}$$
$$\sigma_8 = 0.802^{+0.028+0.055}_{-0.029-0.060} \quad \text{(68.3\%/95.4\% conf., MS-calib.)},$$

which reduces the size of WMAP-only 1σ (2σ) error-bars on average by 21% (27%). We plot the joint and individual constraints in Fig. 15, illustrating the perfect agreement of the two independent cosmological probes.

7. Summary, discussion, and conclusions

We have measured weak lensing galaxy shear estimates from the HST/COSMOS data by applying a new model for the spatially and temporally varying ACS PSF, which is based on a principal component analysis of PSF variations in dense stellar fields. We find that most of the PSF changes can be described with a single parameter related to the HST focus position. Yet, we also correct for additional PSF variations, which are coherent for neighbouring COSMOS tiles taken closely in time. We employ updated parametric corrections for charge-transfer inefficiency, for both galaxies and stars, removing earlier modelling uncertainties due to confused PSF- and CTI-induced stellar ellipticity. Finally, we employ a simple correction for signal-to-noise dependent shear calibration bias, which we derive from the STEP2 simulations of

[12] We expect that this correction factor depends on cosmological parameters. Yet, considering the weak lensing degeneracy for Ω_m and σ_8, the input values of the Millennium Simulation are quasi equivalent to $\sigma_8 \simeq 0.82$ for $\Omega_\mathrm{m} = 0.3$, which is sufficiently close to our constraints to justify the application.
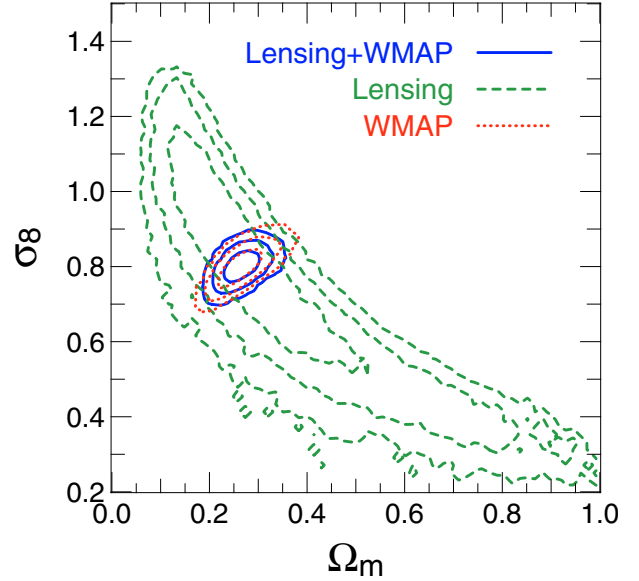

Fig. 15. Comparison of the constraints on Ω_m and σ_8 for a flat ΛCDM cosmology obtained with our COSMOS analysis (dashed), WMAP-5 CMB data (dotted), and joint constraints (solid). The contours indicate the 68.3%, 95.4%, and 99.7% credibility regions. Note that the weak lensing alone analysis uses stronger priors. The weak lensing constraints on σ_8 have been rescaled to account for modelling bias of the non-linear power spectrum and reduced shear corrections according to the ray-tracing constraints from the Millennium Simulation.

ground-based weak lensing data. Tests on simulated space-based data confirm a relative shear calibration uncertainty $|m| \le 2\%$ over the entire used magnitude range if this correction is applied. We decompose the measured shear signal into curl-free E-modes and curl-component B-modes. As expected from pure lensing, the B-mode signal is consistent with zero for all second-order shear statistics, providing an important confirmation for the success of our correction schemes for instrumental systematics.

We combine our shear catalogue with excellent ground-based photometric redshifts from Ilbert et al. (2009) and carefully estimate the redshift distribution for faint ACS galaxies without individual photo-zs. This allows us to study weak lensing cross-correlations in detail between six redshift bins, demonstrating that the signal indeed scales as expected from general relativity for a concordance ΛCDM cosmology.

We employ a robust covariance matrix from 288 simulated COSMOS-like fields obtained from ray-tracing through the Millennium Simulation (Hilbert et al. 2009). Using our 3D weak lensing analysis of COSMOS, we derive constraints $\sigma_8(\Omega_\mathrm{m}/0.3)^{0.51} = 0.79 \pm 0.09$ for a flat ΛCDM cosmology, using non-linear power spectrum corrections from Smith et al. (2003). A recalibration of these predictions based on the ray-tracing analysis changes our constraints to $\sigma_8 \, (\Omega_\mathrm{m}/0.3)^{0.51} = 0.75 \pm 0.08$ (all 68.3% conf.). Our results are perfectly consistent with WMAP-5, yielding joint constraints $\Omega_\mathrm{m} = 0.266^{+0.025+0.057}_{-0.023-0.042}$, $\sigma_8 = 0.802^{+0.028+0.055}_{-0.029-0.060}$ (68.3% and 95.4% confidence). They also agree with weak lensing results from the CFHTLS-Wide (Fu et al. 2008) and recent galaxy cluster constraints from Mantz et al. (2009) within 1σ. Our errors include the full statistical uncertainty including the non-Gaussian sampling variance, Gaussian photo-z scatter, and marginalization over remaining parameter uncertainties, including the redshift calibration for the faint $i^+ > 25$ galaxies.

Our results are consistent with the 3D lensing constraints $\sigma_8(\Omega_m/0.3)^{0.44} = 0.866 \pm 0.033$ (stat.)$^{+0.052}_{-0.035}$ (sys.) from Massey et al. (2007c) assuming non-linear power spectrum corrections according to Smith et al. (2003), at the $\sim 1\sigma$ level. The analyses differ systematically in the treatment of PSF- and CTI-effects, where the success of our methods is confirmed by the vanishing B-mode. Furthermore, Massey et al. (2007c) employ earlier photo-zs based on fewer bands (Mobasher et al. 2007). Note that the analysis of Massey et al. (2007c) yields tighter statistical errors, which may be a result of their covariance estimate from the variation between the four COSMOS quadrants. This potentially introduces a bias in the covariance inversion due to too few independent realizations (Hartlap et al. 2007). While the absolute calibration accuracy of the shear measurement method was estimated to be the dominant source of uncertainty in their error budget, we were able to reduce it well below the statistical error level. As a further difference, our analysis employs photometric redshift information to reduce potential contamination by intrinsic galaxy alignments, where we exclude the shear-shear auto-correlations for the relatively narrow redshift bins 1 to 5 to minimize the impact of physically associated galaxies. In addition, we exclude luminous red galaxies, which were found to carry the strongest intrinsic alignment with the density field of their large-scale structure environment causing the shear (Hirata et al. 2007). Finally, we do not include angular scales $\theta < 0.\!'5$ due to increased modelling uncertainties for the non-linear power spectrum.

Similarly to Massey et al. (2007c), we obtain a lower estimate $\sigma_8(\Omega_m/0.3)^{0.62} = 0.68 \pm 0.11$ for a non-tomographic (2D) analysis, assuming Smith et al. (2003) power spectrum corrections. The lower signal compared to the 3D lensing analysis is expected, given that the most massive structures in COSMOS are located at $0.7 \lesssim z \lesssim 0.9$ (Scoville et al. 2007b), creating a strong shear signal for high redshift sources only, which is detected by the 3D analysis. In contrast, the bulk of the galaxies in the 2D lensing analysis are located at too low redshifts to be substantially lensed by these structures, yielding a relatively low estimate for σ_8. Nonetheless, as sampling variance is properly accounted for in our error analysis, the constraints are still consistent.

For a general (non-flat) ΛCDM cosmology, we find a negative deceleration parameter $q_0 < 0$ at 96.0% confidence using our default priors, and at 94.3% confidence if only priors from the HST Key Project and BBN are applied. Thus, our tomographic weak lensing measurement provides independent evidence of the accelerated expansion of the Universe. For a flat wCDM cosmology we constrain the (constant) dark energy equation of state parameter to $w < -0.41$ (90% conf.) for a prior $w \in [-2, 0]$, fully consistent with ΛCDM. Our dark energy constraints are still weak compared to recent results from independent probes (e.g. Kowalski et al. 2008; Hicken et al. 2009; Allen et al. 2008; Mantz et al. 2008, 2009; Vikhlinin et al. 2009; Komatsu et al. 2009). This is solely due to the limited area of COSMOS, leading to a dominant contribution to the error budget from sampling variance.

While the area covered by COSMOS is still small (1.64 deg^2), the high resolution and depth of the HST data allowed us to obtain cosmological constraints which are comparable to results from substantially larger ground-based surveys. However, note that HST was by no means designed for cosmic shear measurements. In contrast, future space-based lensing mission such as Euclid[13] or JDEM[14] will be highly optimized for weak lensing measurements. High PSF stability, a much larger field-of-view providing thousands of stars for PSF measurements, carefully designed CCDs which minimize charge-transfer inefficiency, and improved algorithms will remove the need for some of the empirical calibrations employed in this paper.

In order to fully exploit the information encoded in the weak lensing shear field, second-order shear statistics, as used here, can be complemented with higher-order shear statistics to probe the non-Gaussianity of the matter distribution (e.g. Bergé et al. 2010; Vafaei et al. 2010). Based on our COSMOS shear catalogue, Semboloni et al. (2010) present such a cosmological analysis using combined second and third-order shear statistics.

Finally, we stress that weak lensing can only provide precision constraints on cosmological parameters if sufficiently accurate models exist to compare the measurements to. Our analysis of the relatively small COSMOS Survey is still limited by the statistical measurement uncertainty, for which our approximate model recalibration using the Millennium Simulation is sufficient. Most of the cosmological sensitivity in COSMOS comes from quasi-linear and non-linear scales. We cut our analysis only at highly non-linear scales $\theta < 0.\!'5$, corresponding to a comoving separation of ~ 360 kpc at $z = 0.7$ (roughly the redshift of the most massive structures in COSMOS). At these scales non-linear power spectrum corrections have substantial uncertainties, in particular due to the influence of baryons (e.g. Rudd et al. 2008). Given that our results are basically unchanged if even smaller scales are included (insignificant increase in σ_8 by $<1\%$), we expect that the model uncertainty for the larger scales should still be sub-dominant compared to our statistical errors. However, analyses of large future surveys will urgently require improved model predictions including corrections for baryonic effects, also for dark energy cosmologies with $w \neq -1$, and optionally also for theories of modified gravity. Once these are available, careful analyses of large current and future weak lensing surveys will deliver precision constraints on cosmological parameters and dark energy properties.

Appendix A: Additional image calibrations

In this appendix we describe additional calibrations which we apply to the flat-fielded _flt images before running `MultiDrizzle`.

Background subtraction. We perform a quadrant-based background subtraction due to an anomalous bias level variation between the four ACS read-out amplifiers. Here we detect and mask objects with `SExtractor` (Bertin & Arnouts 1996), combine this mask with the static bad pixel mask, and estimate the background as the median of all non-masked pixels in the quadrant. We modulate the offset from the mean background level with the normalized inverse flat-field to correct for the fact that the improperly bias-subtracted image has already been flat-fielded[15].

Bad pixel masking. We manually mask satellite trails and scattered stellar light if its apparent sky position changes between different dither positions, allowing us to recover otherwise unusable sky area. In addition, we update the static bad pixel mask rejecting pixels if:

- their dark current exceeds $0.04\,\mathrm{e}^-/\mathrm{s}$ in the associated dark reference file (default $0.08\,\mathrm{e}^-/\mathrm{s}$), or
- they are affected by variable bias structures, which we identify in a variance image of five subsequent bias reference frames taken temporally close to the science frame considered, or
- they show significantly positive or negative values in a median image computed from 50 background-subtracted and object-masked COSMOS frames taken closely in time, indicating any other semi-persistent blemish.

The latter two masks mainly aim at the rejection of variable bias structures which show up as positive or negative bad column segments in the stacked image if not properly masked. For the mask creation we utilize the `IRAF` task `noao.imred.ccdmask`. It computes the local median signal and rms variation in moving rectangles. A pixel is then masked if its values is either `lsigma` below or `hsigma` above the local median value. This is done for individual pixels and sums of pixels in column sections, where in the latter case the background dispersion is scaled by the square root of the number of pixels in the section. Finally each column is scanned for short segments of un-flagged pixels in between masked pixels. We additionally mask these segments if their length is less than 15 pixels. We summarize the values applied for the thresholds `lsigma` and `hsigma` in Table A.1. Due to variations in image noise properties they do not perform optimally in all cases, so that we iteratively increase `hsigma` by +5 if otherwise more than 2.5% of the pixels in the bias variance image would be masked.

---

[15] This procedure performs well for relatively empty fields such as the large majority of the COSMOS tiles. For fields dominated by a very bright star or galaxy, it can, however, lead to erroneous jumps in the background level. Thus, we generally adopt a maximal accepted difference in the background estimates of $4\,\mathrm{e}^-$, which, if exceeded, leads to a subtraction of the minimum background estimate for all quadrants.

Table A.1. Lower and upper σ thresholds for pixel masking with `ccdmask` in the bias variance and the sky-subtracted and object-masked median images.

Image type	lsigma	hsigma
Bias variance	100	25, +5 if more than 2.5% masked
Median, gain = 1	13	11
Median, gain = 2^a	15	15

Notes. [a] The COSMOS images were taken with gain = 1, whereas the gain = 2 setting has been applied for some of the HAGGLeS fields (Marshall et al. 2010, in prep.). While we do not include these fields in the current analysis, they have been processed with the same pipeline upgrades described here. Thus, we list these values for completeness.

Noise model. We compute a rms noise model for each pixel as

$$\mathrm{ERR} = F^{-1}\sqrt{sF + t_{\exp}D + \sigma_r^2 + \gamma^2 V} \quad [\mathrm{e}^-], \tag{A.1}$$

with the normalized flat-field F, the sky background s [e^-], the dark reference frame D [e^-/s], the exposure time $t_{\exp}$ [s], the read-noise $\sigma_r \simeq 5\,\mathrm{e}^-$, and the bias variance image V [counts^2] described in the previous paragraph, which requires scaling with the gain γ [$\mathrm{e}^-/\mathrm{count}$]. Containing all noise sources except object photon noise, this rms model is used for optimal pixel weighting in `MultiDrizzle`.

Appendix B: Correction for PSF and CTI effects

B.1. Summary of our KSB+ implementation

We measure galaxy shapes using the Erben et al. (2001) implementation of the KSB+ formalism (Kaiser et al. 1995; Luppino & Kaiser 1997; Hoekstra et al. 1998), as done in the earlier ACS weak lensing analysis of Schrabback et al. (2007). Object ellipticities[16]

$$e = e_1 + \mathrm{i}e_2 = \frac{Q_{11} - Q_{22} + 2\mathrm{i}Q_{12}}{Q_{11} + Q_{22}} \tag{B.1}$$

are measured from weighted second-order brightness moments

$$Q_{ij} = \int \mathrm{d}^2\theta\, W_{r_g}(|\boldsymbol{\theta}|)\, \theta_i\, \theta_j I(\boldsymbol{\theta}), \quad i,j \in \{1,2\}, \tag{B.2}$$

where W_{r_g} is a 2D Gaussian with dispersion r_g. The response of a galaxy ellipticity to reduced gravitational shear g and PSF effects is given by

$$e_\alpha - e_\alpha^s = P_{\alpha\beta}^g g_\beta + P_{\alpha\beta}^{sm} q_\beta^*, \tag{B.3}$$

with the (seeing convolved) intrinsic source ellipticity e^s and the "pre-seeing" shear polarizability

$$P_{\alpha\beta}^g = P_{\alpha\beta}^{sh} - P_{\alpha\gamma}^{sm}\left[(P^{sm*})_{\gamma\delta}^{-1} P_{\delta\beta}^{sh*}\right], \tag{B.4}$$

where the shear and smear polarizability tensors P^{sh} and P^{sm} are calculated from higher-order brightness moments as detailed in Hoekstra et al. (1998). The PSF anisotropy kernel $q_\alpha^* = (P^{sm*})_{\alpha\beta}^{-1} e_\beta^*$ and ratio of P^{sh*} and P^{sm*} must be measured from stars and interpolated for each galaxy position, where we approximate the latter as $T^* = \mathrm{Tr}\left[P^{sh*}\right]/\mathrm{Tr}\left[P^{sm*}\right]$.

---

[16] We adopt the widely used term "ellipticity" here, but note that, strictly speaking, (B.1) corresponds to the definition of the polarization.

In the application of the KSB+ formalism several choices lead to subtle differences between different KSB implementations, see Heymans et al. (2006a) for a detailed comparison. In short, we use sub-pixel interpolation for integral evaluations, measure galaxy shapes with $r_g = r_f$, the SExtractor flux-radius, and apply PSF measurements computed with the same filter scale as used for the corresponding galaxy (interpolated between 24 values with $1 \leq r_g \leq 15$ pixels). We invert the P^g tensor as measured from individual galaxies using the approximation $(P^g)^{-1} = 2/\text{Tr}[P^g]$ commonly applied to reduce noise (Erben et al. 2001). In contrast to Schrabback et al. (2007) we do not apply a constant calibration correction, but employ the signal-to-noise dependent correction (6).

B.2. Tests with simulated space-based data

We test our KSB+ shape measurement pipeline on simulated space-based weak lensing data with ACS-like properties, which were provided for testing in the framework of the Shear Testing Programme[17]. The images were created with the Massey et al. (2004) image simulation pipeline, which uses shapelets (Refregier & Bacon 2003; Massey & Refregier 2005) to model galaxy and PSF shapes, as already employed for the STEP2 simulations (Massey et al. 2007a). All images have 4k × 4k pixels of size 0″.04, HST-like resolution, and a depth equivalent to 2ks of ACS imaging. The data are subdivided into eight sets with different PSFs ($|e^*| \lesssim 7\%$), seven of which utilize TinyTim[18] ACS PSF models, and one was created by stacking stars of similar ellipticity in an ACS stellar field (M). One of the sets uses simplified exponential profiles for galaxy modelling (F), while the others include complex galaxy morphologies modelled with shapelets. Four sets comprise 100 images, while the others include 200 frames. Within each set, the images are split into "rotated pairs", where the intrinsic galaxy ellipticities in one frame resemble 90 degree-rotated versions from the other frame, an approach used in Massey et al. (2007a) to reduce the analysis uncertainty due to shape-noise. Galaxies are sheared with $|g| < 0.06$ and convolved with the PSF, both effects being constant within one frame, but with varying g within one set. Realistic image noise was added similarly to the STEP2 analysis, except that no noise correlations were introduced.

We analyse the images with the same pipeline and cuts as the real COSMOS data, with the only difference that the PSF is assumed to be constant across the field, but still measured from the simulated stars. Figure B.1 shows the mean calibration bias m and PSF anisotropy residuals c defined in (5), separately for each image simulation set, estimated from matched galaxy pairs (for details on this fit see Massey et al. 2007a). While some data sets deviate from the optimal $m = c = 0$, the residuals are at a level which is negligible compared to the statistical uncertainty of COSMOS. Combining all sets and both shear components, we estimate the mean calibration bias $m = +0.008 \pm 0.002$, and the scatter of the PSF anisotropy residuals $\sigma_c = 0.0006$.

As discussed in Sect. 3, a possible magnitude-dependence of the shear calibration bias m is particularly problematic for 3D weak lensing studies. We therefore study m as a function of magnitude in Fig. B.2, both for the simulated ground-based STEP2 and the simulated space-based ACS-like data. Although the applied correction (6) was determined from the simulated ground-based data, it also performs very well for the ACS-like simulations, showing its robustness. Over the entire magnitude range
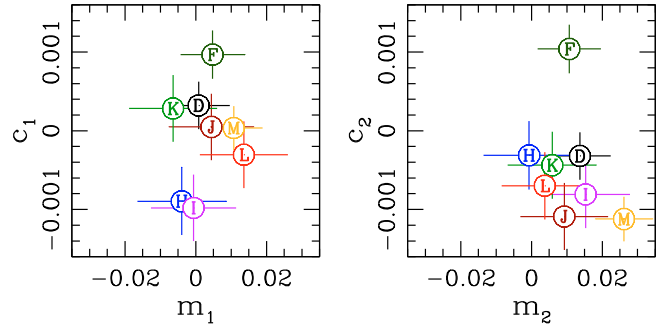

Fig. B.1. Shear calibration bias m and PSF anisotropy residuals c as measured in the simulated ACS-like lensing data. The *left* and *right* panels show the results for the γ_1 and γ_2 shear components respectively. Each letter corresponds to a different PSF model. Although some data sets deviate from the optimal $m = c = 0$, the residuals are at a level which is negligible compared to the statistical errors for COSMOS.
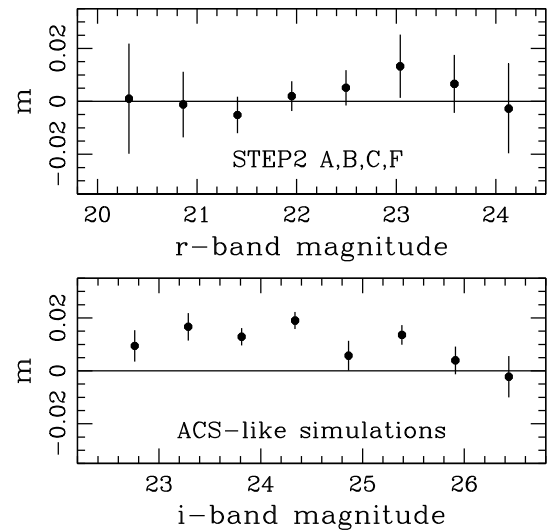

Fig. B.2. Magnitude-dependence of the shear calibration bias for our KSB implementation after correction for S/N-dependent bias according to (6). The *top* panel shows results for the STEP2 simulations of ground-based lensing data (Massey et al. 2007a), which have been used to derive (6), where we have excluded the untypically elliptical PSFs D and E. The *bottom* panel shows the remaining calibration bias for the ACS-like simulations of space-based lensing data. In both panels we plot the average computed from all PSF models and the two shear components, with error-bars indicating the uncertainty of the mean. Despite the very different characteristics of the two sets of simulations, (6) performs also very well for the ACS-like data, with a bias $|m| \leq 0.02$ over the entire magnitude range. The remaining calibration uncertainty is negligible compared to the statistical errors for COSMOS.

the remaining calibration bias is $|m| \leq 0.02$, which is negligible compared to our statistical errors.

B.3. Stellar fields

We have analysed 700 i_{814} exposures of dense stellar fields, which were taken between 2002 Apr. 18 and 2006 Jun. 3 and contain at least 300 non-saturated stars with $S/N > 50$ (for $r_g = 1.5$ pixels). This large set enables us to study in detail the impact of CTI on stars, as well as the temporal and positional ACS PSF variation, which cannot be achieved from the COSMOS exposures due to their low stellar density.

---

[17] http://www.physics.ubc.ca/~heymans/step.html
[18] http://www.stsci.edu/software/tinytim/

We determine both CTI and PSF models for the cosmic ray-cleansed *COR* images before resampling, and their resampled (but not stacked) counterparts (*DRZ*). The reason is that resampling unavoidably adds extra noise. Therefore it is best to fit the available stars in a galaxy field exposure before resampling. Yet, the combined PSF model for a stack has to be determined from resampled image models according to the relative dithering. For the *COR*-image analysis we employ a fixed Gaussian filter scale $r_g = 1.5$ pixels, in order to maximize the fitting signal-to-noise (see Schrabback et al. 2007), and characterize the PSF by the ellipticity e^*_α and stellar half-light radius r^*_h as suggested by Jee et al. (2007). For the *DRZ* images we require CTI-corrected PSF models for all 24 values of r_g used for the galaxy correction.

B.4. Stellar CTI correction

CTI charge trails stretch objects in the readout y-direction, leading to an additional negative e_1 ellipticity component. Internal calibrations (Mutchler & Sirianni 2005), photometric studies (e.g. Chiaberge et al. 2009), as well as the analysis of warm pixels (Massey et al. 2010) and cosmic rays (Jee et al. 2009) demonstrate that the influence of CTI increases linearly with time and the number of y-transfers, where the latter has also been shown for the influence on galaxy ellipticities by Rhodes et al. (2007). In addition, the limited depth of charge traps leads to a stronger influence of CTI for faint sources, which lose a larger fraction of their charge than bright sources. Likewise, the effect is reduced for higher sky background values leading to a fraction of continuously filled traps. Here we only study the effect of CTI on stars, whereas galaxies will be considered in Appendix B.6.

Following Chiaberge et al. (2009), we assume a power-law dependence on sky background and integrated flux as measured in apertures of $4.5\, r_f \simeq 5.8$ pixels, leading to the parametric CTI model

$$e^{cti,*}_1(r_g) = -e^0_1(r_g)\left(\frac{FLUX}{10^4 e^-}\right)^{-F(r_g)}\left(\frac{SKY}{30 e^-}\right)^{-S(r_g)}\left(\frac{t}{1000 d}\right)$$
$$\times \left(\frac{y_{trans}}{2048}\right), \tag{B.5}$$

with the time $t = MJD - 52\,340$ since the installation of ACS on 2002 Mar. 08, and the number of y-transfers y_{trans}. We expect that the normalization $e^0_1(r_g)$ and power law exponents $F(r_g)$ and $S(r_g)$ depend on the Gaussian filter scale r_g of the KSB ellipticity measurement. E.g., for a measurement of the PSF core with small r_g, charge traps may already be filled by electrons from the outer stellar profile, leading to an expected strong flux-dependence. On the contrary, the PSF wings measured at large r_g will be more susceptible to trap filling by background electrons, leading to a stronger sky-dependence.

In order to separate CTI and PSF effects we make use of the fact that CTI-induced ellipticity is expected to depend on flux, while PSF ellipticity is flux-independent. In our analysis of stellar field exposures we first fit the spatial ellipticity variation of bright non-saturated stars with $S/N > 50$ using a third-order polynomial in each chip, and apply this model to all stars with $S/N > 5$. For the high S/N stars used in the fit, the strongest ellipticity contribution comes from the spatially varying PSF. Yet, for these stars the polynomial fit also corrects for the position-dependent but *flux-averaged* CTI effect, leading to a net negative e_1 ellipticity for fainter than average stars (CTI under-corrected), and net positive e_1 for brighter stars (CTI over-corrected). For even fainter stars with $S/N < 50$ we expect an increasingly more negative e_1 ellipticity component. Thus, the CTI influence can be
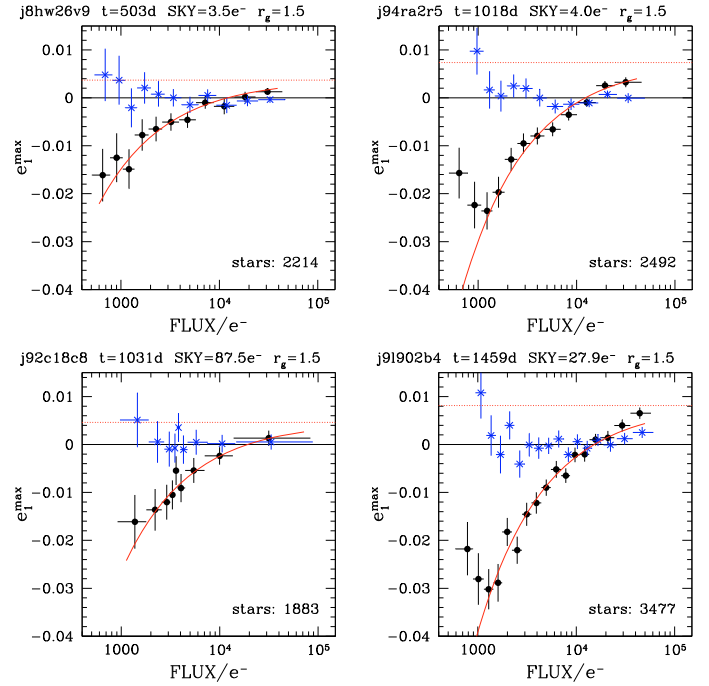

Fig. B.3. CTI-induced stellar ellipticity for four example stellar field exposures: The bold points show the mean stellar e_1 ellipticity-component as a function of stellar flux after subtraction of a spatial third-order polynomial model derived from bright stars ($S/N > 50$) to separate PSF and CTI effects. Each stellar ellipticity has been scaled to a reference number of $y_{trans} = 2048$ parallel readout transfers. The curves show the CTI model (B.5), where the fit parameters have been jointly determined from $S/N > 20$ stars in all 700 exposures, and an offset shown by the horizontal line has been applied, corresponding to the mean CTI model ellipticity of the bright stars used for the polynomial interpolation. The crosses indicate the corrected ellipticities after subtraction of the CTI model. Note the strong increase of the CTI-induced ellipticity with time (*top left* to *bottom right*) and moderate dependence on sky background (*top right* versus *bottom left* at similar times). Also note the turnaround occurring for faint stars at $\sim 1000 e^-$ (corresponding to $S/N \sim 5-10$) in the *right* panels, see Jee et al. (2009) for a further investigation of this effect. The plots shown correspond to the non-resampled *COR*-images with ellipticities measured using a Gaussian filter scale of $r_g = 1.5$ pixels.

measured from the flux-dependence of the polynomial-corrected *residual* ellipticity, as illustrated in Fig. B.3 for four example exposures. We note a turnaround in the CTI flux-dependence for some exposures at low $S/N \sim 5 - 10$ (right panels in Fig. B.3), which was also reported for CTI measurements from cosmic rays and further investigated by Jee et al. (2009). This does not affect our stellar models, given that we only use $S/N > 20$ stars both for PSF measurement and to constrain (B.5). Yet, it suggests that CTI models may not be valid over very wide ranges in signal-to-noise, motivating the use of a separate model for the typically much fainter galaxies in Appendix B.6.

We determine the three fit parameters in (B.5) jointly from the polynomial-corrected residual ellipticities in all stellar exposures. For each exposure it is necessary to add an offset, which has been linearly scaled with y_{trans} for each star, in order to compensate for the flux-averaged correction included in the polynomial fit. We compute this offset within the non-linear fitting routine[19] for a given set of fit parameters from the positions and

---

[19] For the non-linear CTI fits we utilize the CERN Program Library MINUIT: http://wwwasdoc.web.cern.ch/wwwasdoc/minuit/.
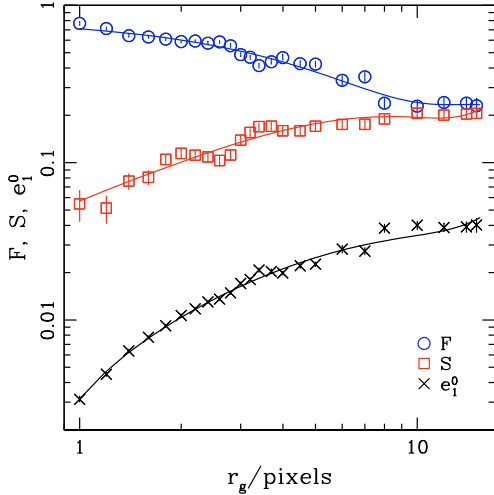
Fig. B.4. Dependence of the best fitting parameters of the stellar CTI model (B.5) on the Gaussian filter scale r_g used for shape measurements in the resampled *DRZ*-images. The curves correspond to the fitting functions (B.6).

Table B.1. Fitted coefficients for the r_g-dependent CTI-ellipticity model (B.6) in the resampled *DRZ* frames.

j	a_j	b_j	c_j
0	-5.623×10^{-3}	8.371×10^{-1}	1.417×10^{-3}
1	9.573×10^{-3}	-1.372×10^{-1}	6.182×10^{-2}
2	-8.307×10^{-4}	1.037×10^{-2}	-6.410×10^{-3}
3	2.739×10^{-5}	-2.597×10^{-4}	2.155×10^{-4}

fluxes of the bright stars used in the polynomial fit, and apply it to all stars.

We conduct this fit both for the *COR*-image ellipticities ($r_g = 1.5$) yielding best fitting values $(e_1^0, F, S) = (0.0073 \pm 0.0002, 0.65 \pm 0.02, 0.06 \pm 0.01)$, and for the resampled *DRZ*-images for all values of r_g. For the latter we adjust the S/N cuts in order to keep enough stars for large r_g. The best fit values are shown in Fig. B.4 as function of r_g, indeed confirming the expected trends. We provide the fitting functions

$$e_1^0(r_g) = \sum_{j=0}^{j=3} a_j r_g^j, \quad F(r_g) = \sum_{j=0}^{j=3} b_j r_g^j, \quad S(r_g) = \sum_{j=0}^{j=3} c_j r_g^j, \quad (B.6)$$

where the coefficients are listed in Table B.1, being valid for $1 \leq r_g \leq 15$ pixels. We correct the ellipticities of all stars both in the stellar and galaxy fields with the derived models, as implicitly assumed in the following sections.

B.5. Principal-component correction for the time-dependent ACS PSF

As discussed in Sect. 3, ACS PSF variations are expected to be mostly caused by changes in telescope focus (e.g. Krist 2003; Lallo et al. 2006; Anderson & King 2006). If the temporal variations indeed depend on one physical parameter only, it should be possible to construct a one-parametric PSF model, which can be well constrained with the ~10−20 stars available in an ACS field at high galactic latitudes. Such an approach was implemented by Rhodes et al. (2007), who measure the mean focus offset for a COSMOS stack from simulated focus-dependent `TinyTim` PSF

models. They then interpolate the ACS PSF between all stars in COSMOS using polynomial functions dependent on both position and focus offset (Leauthaud et al. 2007; Massey et al. 2007c). However, as suggested by the residual aperture mass B-mode signal found by Massey et al. (2007c), this approach appears to be insufficient for a complete removal of systematics. In an alternative approach, Schrabback et al. (2007) fit the stars present in each galaxy field exposure using a large library of stellar field PSF models. While this approach led to no significant residual systematics within the statistical accuracy of GEMS, it is also not sufficient for the analysis of the much larger COSMOS data set. We therefore implement a new PSF interpolation scheme based on principal component analysis. It effectively combines the idea of exposure-based empirical models, which optimally account for time variations and relative dithering (Schrabback et al. 2007), with the aim to describe the PSF variation with a single parameter (Rhodes et al. 2007).

Jarvis & Jain (2004) introduced the application of principal component analysis (PCA) for ground-based PSF interpolation, which we adapt here to obtain well-constrained PSF models for our ACS weak lensing fields. Note that Jee et al. (2007) and Nakajima et al. (2009) employed PCA to efficiently describe the two-dimensional ACS PSF shape, which they then spatially interpolated with normal polynomial functions. This is conceptually very different to the approach suggested by Jarvis & Jain (2004) and used here, which employs PCA for the spatial and temporal interpolation of certain quantities needed for PSF correction, such as the stellar ellipticity e^*.

We represent all quantities which we want to interpolate as p_α. This includes e_1^*, e_2^*, r_h^* measured in the *COR* images for $r_g = 1.5$ pixels, but also $e_1^*, e_2^*, q_1^*, q_2^*, T^*$ as measured in the *DRZ* images for varying r_g. The only exception is when we specifically allude to *COR* quantities, which only includes the first group.

The first step of the PCA analysis is to fit the positional variation of the three *COR* PSF quantities in all $j \leq N = 700$ stellar exposures jointly for both chips with 3rd-order polynomials

$$P_{\alpha,j}^{(3)}(\hat{x}, \hat{y}) = \sum_{i=1}^{m} d_{ij} \hat{x}^{\mu_i} \hat{y}^{\nu_i}, \quad (B.7)$$

yielding $m = 10$ coefficients each, where we generally denote polynomials using a capital P with the order indicated by the superscript. Here we account for the gap between the chips and rescale the pixel range to the interval $\hat{x}, \hat{y} \in [0, 1]$. While this fit is unable to account for some small-scale features such as a small discontinuity between the two chips, it captures all major large-scale PSF variations and is very well constrained by the required ≥ 300 stars. For each exposure we arrange the $M = 3 \times m = 30$ polynomial coefficients in a data vector $\mathbf{d}_j$, with components d_{ij} (now $i \leq M$). We then subtract the mean vector and divide each component with an adequately chosen normalization n_i, yielding the modified data vector $\hat{\mathbf{d}}_j$ with

$$\hat{d}_{ij} = \frac{d_{ij} - \overline{d_i}}{n_i} . \quad (B.8)$$

We then arrange all modified data vectors into a $M \times N$ dimensional data matrix $\mathbf{D} = \{\hat{\mathbf{d}}_1, ..., \hat{\mathbf{d}}_N\}$. The central step of the PCA is a singular value decomposition $\mathbf{D} = \mathbf{W}\Sigma\mathbf{V}^T$, where the orthonormal matrix $\mathbf{W}$ consists of the singular vectors of $\mathbf{D}$, and the diagonal matrix Σ contains the ordered singular values s_{ll} of $\mathbf{D}$ as diagonal elements. Here the lth largest singular value corresponds to the lth singular vector, which is also named the lth

principal component. In the coordinate system spanned by the singular vectors, the matrix $C = DD^{T} = W\Sigma\Sigma^{T}W^{T} = W\Lambda W^{T}$ corresponding to the covariance matrix for $n_i = 1$, becomes diagonal, where the sorted eigenvalues $\lambda_l = s_{ll}^2$ are equal to the variance of the vectors $\hat{d}_j$ along the direction of the lth principal component.

Note that the relative values and absolute scale of the eigenvalues λ_l depend on the normalizations n_i. Uniform $n_i = 1$ would not be adequate given that we combine PSF quantities with different units (dimensionless e_α^* versus r_h^* in pixels). A correlation analysis with $n_i = \sigma_i = \sqrt{\sum_{j=1}^{N}(d_{ij} - \overline{d_i})^2/N}$ could be used, but here relatively stable polynomial coefficients with small σ_i would unnecessarily add noise, effectively increasing the relative eigenvalues of higher principal components. Aiming at a compact description of most of the actual PSF variation in the field with a small number of important principal components, we employ the normalization

$$n_i = (\mu_i + 1)(\nu_i + 1)\sigma_\alpha, \tag{B.9}$$

where we use the mean variance of all coefficients belonging to the corresponding PSF quantity p_α:

$$\sigma_\alpha^2 = \frac{1}{m}\sum_{i=i_{\min,\alpha}}^{i_{\max,\alpha}}\frac{1}{N}\sum_{j=1}^{N}(d_{ij} - \overline{d_i})^2. \tag{B.10}$$

In this way the $\hat{d}_{ij}$ in (B.8) become dimensionless, all three PSF quantities contribute similarly to the total variation, and the undesired noise from relatively stable polynomial coefficients is avoided, as their variation is averaged with that from the less stable coefficients. The pre-factor in (B.9) equals the inverse of the integral $\int_0^1 d\hat{x}\, d\hat{y}\, \hat{x}^{\mu_i}\hat{y}^{\nu_i}$ of the corresponding polynomial term in (B.7). It accounts for our aim to scale according to the actual PSF variation, where e.g. a 0th-order term affects the whole field while a 3rd-order term with similar amplitude gets lower weight as it contributes substantially in a smaller area only.

We plot the fractional eigenvalues in Fig. B.5, once using the analysis as described above (solid curve) and once considering only the two ellipticity components without r_h^* (dashed curve). In both cases the first principal component is clearly dominant, contributing with 95% (97%) of the total variance. We identify this variation as the influence of focus changes, which are expected to dominate the actual PSF variation. The reason why the second principal component has a larger eigenvalue if r_h^* is included in the analysis (fractional $\lambda_2 = 1.1\%$ versus $\lambda_2 = 0.6\%$) can be seen if we project the data variation onto the space spanned by the singular vectors $Y = W^T D$, with components y_{lj}. Looking at the $y_{1j} - y_{2j}$ variation in the left panel of Fig. B.6, where r_h^* has been included, we see that the data points roughly follow a quadratic curve in the plane defined by the first two singular vectors. The reason for this is the linear response of PSF ellipticity on defocus caused by astigmatism, while PSF width responds to leading order quadratically (see e.g. Jarvis et al. 2008). Given that PCA is a purely linear coordinate transformation, it is not capable to directly capture this one-parametric variation (separation between primary and secondary mirror) with a single principal component. This is only possible if PSF quantities with the same dependence on physical parameters are included, hence the smaller λ_2 if only the two ellipticity components are considered. Thus, for other applications it might be more favourable to perform a PCA analysis for each considered PSF quantity separately, as also done by Jarvis & Jain (2004). Yet, here we want to include the extra information encoded in the r_h^* variation to constrain the
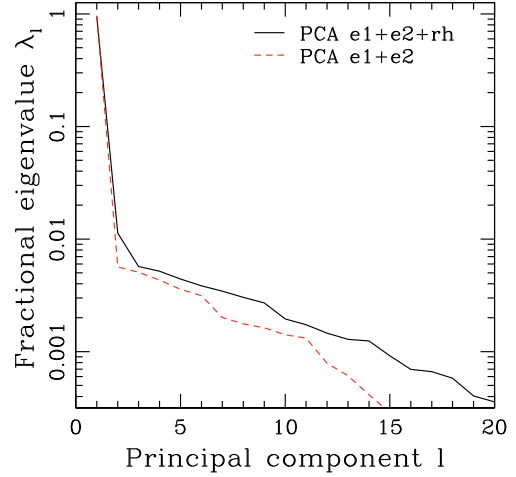

Fig. B.5. Fractional PCA eigenvalues for the PSF variation in 700 i_{814} ACS stellar field exposures. The dashed (solid) curve has been computed considering the variation of e_1^* and e_2^* (e_1^*, e_2^*, and r_h^*). The dominant first principal component contains 97% (95%) of the variation and is caused by focus variations.

galaxy field PSF models, and will therefore account for the non-linear dependence below. The mean stellar half-light radius in each exposure, $\overline{r_h^*}$ is plotted as a function of the first principal component coefficient in Fig. B.7, showing that a fourth-order polynomial fit is capable to describe the full non-linear variation.

In order to obtain a well constrained model for all p_α with high spatial resolution, we jointly fit all stars from all $j \leq N$ exposures with a model

$$p_{\alpha,j,\text{chip}}^{\text{pcafit}}(\hat{x}, \hat{y}) = \sum_{l=0}^{l_{\max}}\sum_{c_l=1}^{c_{l,\max}}[y_{lj}]^{c_l} P_{\alpha,\text{chip},l,c_l}^{(5)}(\hat{x}, \hat{y}), \tag{B.11}$$

separately for both chips, where $P_{\alpha,\text{chip},l,c_l}^{(5)}(\hat{x}, \hat{y})$ indicates a fifth-order polynomial in the corresponding rescaled $\hat{x}, \hat{y}$ coordinates, and $l = 0$ with $c_{0,\max} = 1$ and $y_{0j} = 1$ corresponds to the subtracted mean data vector, now modelled with high spatial resolution. We aim to fit the few stars in the galaxy fields with as few parameters as reasonably possible. Due to the dominant role of focus changes we therefore use only the first principal component in our analysis $l_{\max} = 1$, but include up to fourth-order terms ($c_{1,\max} = 4$) in y_{1j}. This takes out the non-linear distortion visible in Figs. B.6 and B.7, and hence the bulk of the variation in the second principal component. This combination yields a total of $(1 + 4) \times 21 = 105$ coefficients per PSF quantity and chip, which are very well constrained from a total of 5×10^5 stars per chip.

For illustration we plot the field-of-view dependence of the high-resolution *DRZ* ellipticity model measured for $r_g = 1.4$ pixels in Fig. B.8, where the left panel shows the mean PSF ellipticity ($l = 0$), while the right panel depicts the first singular vector ($l = 1$). Note the slight discontinuity of the mean PSF ellipticity between the chips, which is likely caused by small height differences between the CCDs as reported by Krist (2003). See also Rhodes et al. (2007) who measure a stronger discontinuity in the TinyTim PSF model but not for stars in COSMOS, and Jee et al. (2007) who notice it in the PSF size but not ellipticity variation.

To obtain PSF models for our COSMOS stacks, we fit e_1^*, e_2^*, r_h^* of all stars in the single COSMOS *COR* exposures with the PCA model (B.11) to determine the first principal
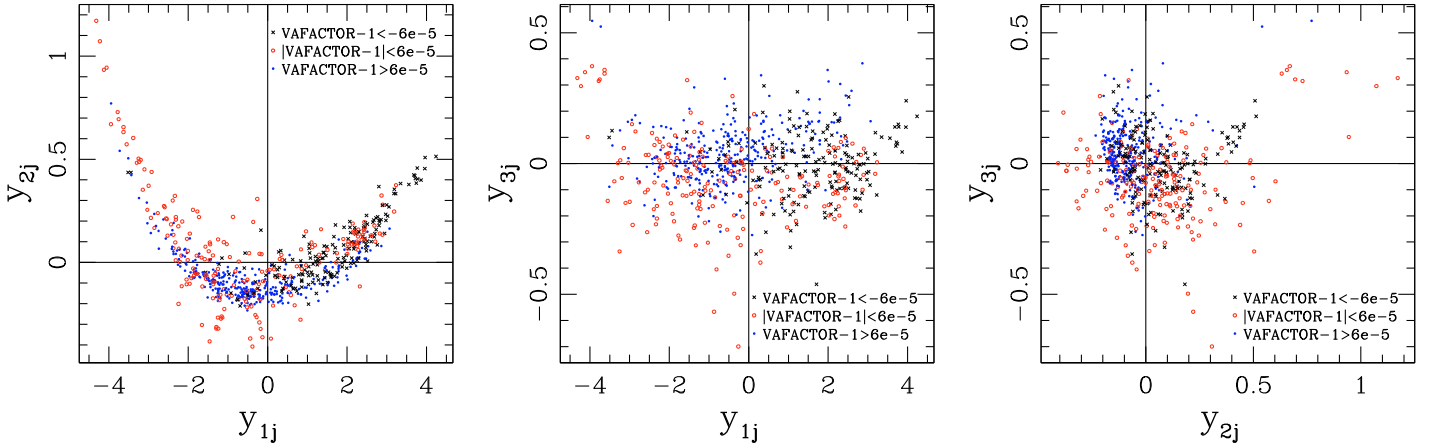
Fig. B.6. Variation of 700 i_{814} stellar field exposures in the space spanned by the first three principal components, which have been computed using the polynomial coefficients of e_1^*, e_2^*, and r_h^*. Note the different axis scales. The non-linear dependence in the *left panel* is caused by the different response of PSF ellipticity and size on defocus, and leads to the increased eigenvalue λ_2 in Fig. B.5 if the r_h^* variation is included in the PCA. The data points have been split according to the velocity aberration plate scale factor VAFACTOR. The fact that the three subsets scatter differently for fixed y_{1j} shows that deviations from pure focus variations are not completely random, but depend on orbital parameters and may hence be coherent for surveys such as COSMOS.
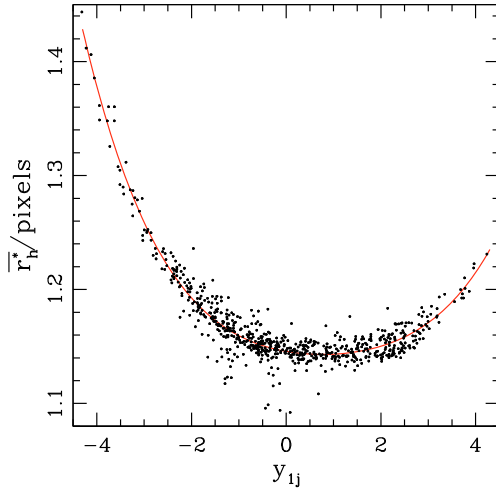

Fig. B.7. Mean stellar half-light radius $\overline{r_h^*}$ as a function of the first principal component coefficient y_{1j} for the 700 i_{814} stellar field exposures. At $y_{1j} \simeq 1$ the telescope is optimally focused. The curve shows the best fitting fourth-order polynomial fit. The outliers are caused by crowded fields with very broad stellar locus.

component coefficient y_{1j} for this exposure. We then average the corresponding *DRZ*-image PSF models of all exposures contributing to a tile, taking their relative dither offsets and rotations into account, as detailed in Schrabback et al. (2007).

We plot the time dependence of the estimated coefficient y_{1j} for both the COSMOS and stellar field exposures in Fig. B.9. Note that HST has been refocused at several occasions to compensate long-term shrinkage of the OTA, with one correction by +4.2 microns being applied during the time-span of the COSMOS observations on 2004 Dec. 22[20]. To ease the comparison, all plots shown in Figs. B.5 to B.9 have been created using a single PCA model determined from all star fields. Yet, to exclude any possible influence of the refocusing, we actually use separate (but very similar) PCA models for the two epochs in our weak lensing analysis.

While the fit (B.11) captures ~97% of the total PSF variation in the stellar fields and metric defined above, it is important to realize that further PSF variations beyond focus changes do actually occur. These are indicated by the higher principal components and the additional scatter beyond the curved distortion in the second principal component. The subdivision of fields according to the velocity aberration plate scale factor VAFACTOR in Fig. B.6, which depends on the angle between the pointing and the telescope orbital velocity vector (see e.g. Cox & Gilliland 2002), indicates that these distortions are not random but may be coherent for neighbouring fields observed under similar conditions. This is not surprising given that HST undergoes substantial temperature changes and the relative angle towards the sun may lead to pointing-dependent effects[21]. For a survey like COSMOS, where neighbouring fields have often been observed under similar conditions, we thus expect coherent residual PSF distortions beyond the one-parameter model introduced here.

These residuals cannot be constrained reliably from the few stars present in a single ACS galaxy field, as one would have to fit ≳10 principal components given the slow decline of the $l \geq 3$ eigenvalues (Fig. B.5). However, under the assumption that they are semi-stable for fields observed under similar conditions, we can constrain these PSF residuals by combining the stars of multiple COSMOS tiles taken closely in time.

For this purpose, we split the COSMOS fields into 24 epochs. Within each epoch the data were taken closely in time, with the same orientation and similar sun angles. The only exception are two tiles which were reobserved between 2005 Oct. 28 and 2005 Nov. 24 due to previous guide-star failures (Koekemoer et al. 2007), which we add to epochs observed one year earlier under similar conditions. Within each epoch we combine the stars of all tiles and compute residuals of the *DRZ* image PSF quantities e_1^*, e_2^*, q_1^*, q_2^*, T^* by correcting their values measured from the stacks with the (dithered and averaged) models (B.11). We then fit these *residuals* as

$$p_{\alpha,j}^{\text{resfit}}(\hat{x}, \hat{y}) = P_{\alpha,0}^{(2)}(\hat{x}, \hat{y}) + \overline{y_{1j}} P_{\alpha,1}^{(2)}(\hat{x}, \hat{y}) \qquad (B.12)$$

---

[21] Note that the actual impact of velocity aberration on object shapes is negligible for our analysis, as long as it is properly accounted for in the image stacking, as done by MultiDrizzle.
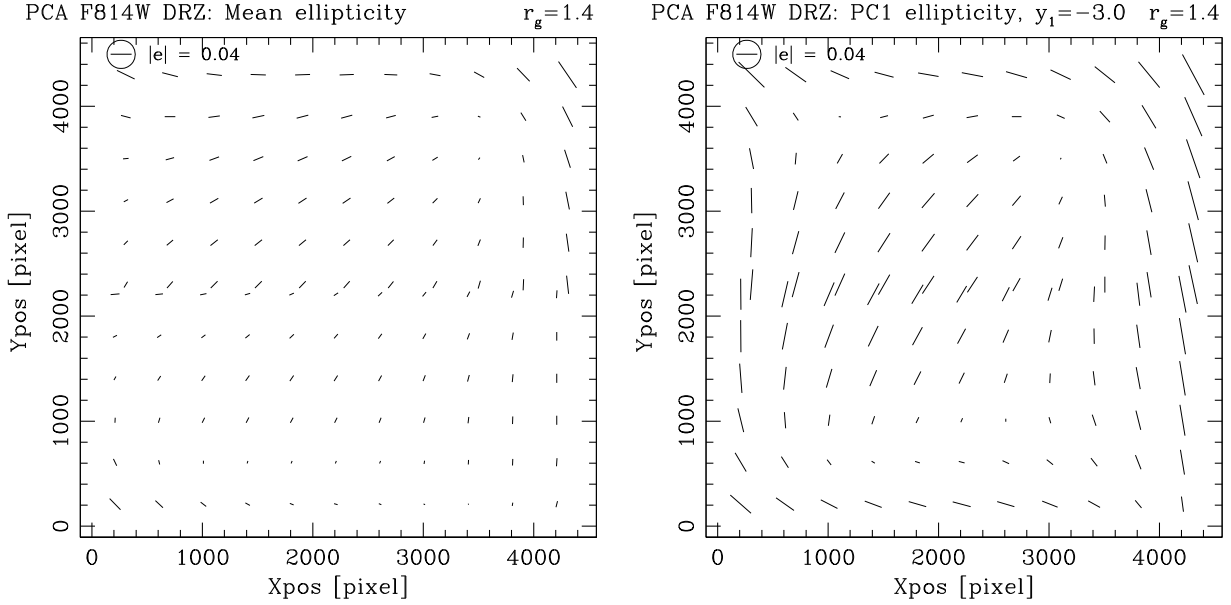
Fig. B.8. PCA PSF model (B.11) for the *DRZ* field-of-view ellipticity variation measured with $r_g = 1.4$ pixels. The *left panel* shows the mean ellipticity ($l = 0$), whereas the *right panel* depicts the first singular vector ($l = 1$, $c_l = 1$) which corresponds to focus changes, for an arbitrary scale $y_1 = -3.0$ (for positive y_1 the ellipticities are rotated by 90°).
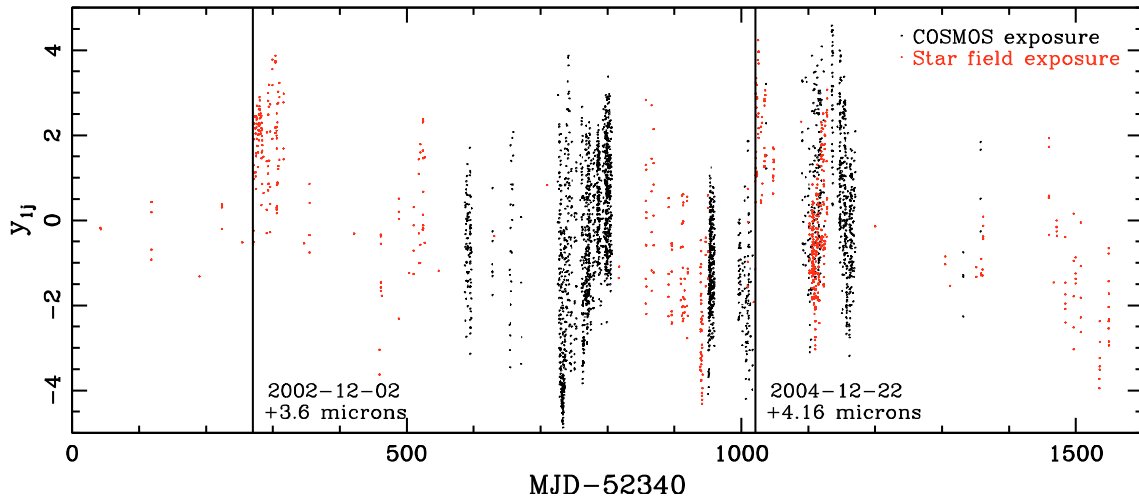

Fig. B.9. Temporal variation of the first principal component coefficient y_{1j}, which is related to the HST focus position, measured in the stellar field and COSMOS exposures. The long-term shrinkage of the OTA is well visible as a decrease in the mean y_{1j}, which was compensated with the marked focus adjustments. The wide spread at a given date is not caused by measurement errors but orbital breathing leading to substantial short-term focus variations.

where $\overline{y_{1j}}$ has been averaged between the four exposures contributing to the stack j, and $P_{\alpha,0}^{(2)}$ and $P_{\alpha,1}^{(2)}$ indicate second-order polynomials in the rescaled coordinates $\hat{x}$, $\hat{y}$ determined for both chips together. Here we assume that the additional PSF variations are in principle stable during each epoch, but their impact might depend on the actual focus position and hence $\overline{y_{1j}}$. Note that we do not use higher-order polynomials in $\hat{x}$, $\hat{y}$ or non-linear powers of $\overline{y_{1j}}$, as we would otherwise risk over-fitting for epochs with few contributing exposures. Yet, we tested slightly higher orders for those epochs containing sufficiently many stars, yielding nearly unchanged results. In general we found that the fitted coherent PSF residuals are small, with a mean rms model ellipticity of 0.3% (for $r_g = 1.4$ pixels). However, some epochs showed somewhat enhanced ellipticity residuals, with two examples given in Fig. B.10, motivating us to include this extra term in the galaxy PSF correction. In contrast we found that the residuals

for T^* are negligible. Also note that we deviate from our philosophy to obtain purely exposure-based models at this point, which is justified by the small and smooth (low-order) corrections applied, which are only marginally affected by dithering.

B.6. Galaxy correction and selection

We measure galaxy shapes and correct for PSF effects as detailed in the previous subsections. We then select galaxies with cuts $r_h > 1.2 r_h^{*,max}$, where $r_h^{*,max}$ is the maximum half-light radius of the 0.25 pixel wide, automatically determined stellar locus in the image, $S/N > 2.0$, and $\text{Tr}[P^g]/2 > 0.1$, identical to the cuts applied to the simulated data in Appendix B.2. We also reject saturated stars and galaxies containing masked pixels (Sect. 2). In order to correct galaxy shapes for spurious CTI ellipticity, we fit the PSF anisotropy-corrected galaxy ellipticity component
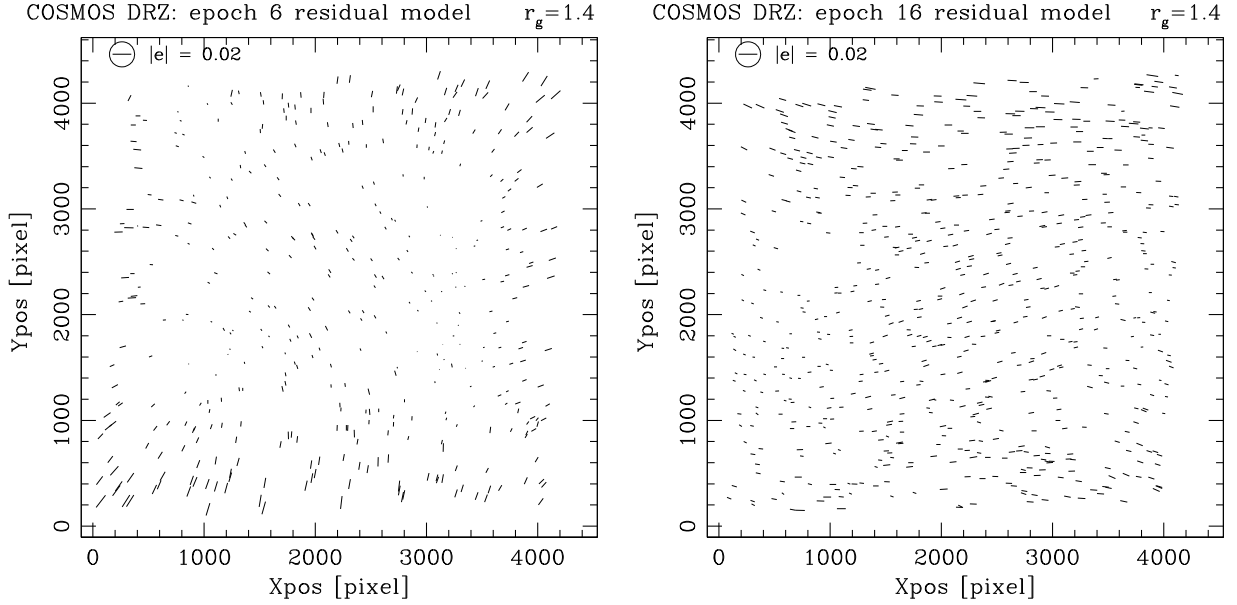
Fig. B.10. Examples for the residual ellipticity model (B.12) determined after subtraction of the 1-parametric PCA model (B.11) from the stellar ellipticities measured in COSMOS stacks with $r_g = 1.4$ pixels. The *left* (*right*) plot has been determined from all COSMOS fields with $732 < t < 735$ $(950 < t < 954.5)$, where $t = \text{MJD} - 52340$. Each whisker represents the residual ellipticity model for one star in the epoch. In some cases the model appears to be discontinuous due to the dependence on $\overline{y_{1j}}$ or focus. Note the different scale compared to Fig. B.8.

$e_1^{\text{ani}} = e_1 - P_{1\beta}^{\text{sm}} q_\beta^*$ with the power law model

$$e_1^{\text{cti,gal}} = -e_1^0 \left(\frac{\text{FLUX}}{10^3 \text{e}^-}\right)^{-F} \left(\frac{r_f}{3\,\text{pixel}}\right)^{-R} \left(\frac{\text{SKY}}{30\text{e}^-}\right)^{-S}$$
$$\times \left(\frac{t}{1000\text{d}}\right)\left(\frac{y_{\text{trans}}}{2048}\right), \tag{B.13}$$

with the mean sky level of the contributing exposures SKY, the time $t = \text{MJD} - 52340$ since the installation of ACS, the number of y-transfers y_{trans}, the SExtractor flux-radius r_f (FLUX_RADIUS), and the mean integrated flux per exposure $\text{FLUX} = \overline{t_{\text{exp}}} \cdot \text{FLUX\_AUTO}$ measured by SExtractor. We scale the latter with the mean exposure time per exposure as the stacks are in units of e^-/s. This model is similar to the one employed by Rhodes et al. (2007), but additionally accounts for the sky background-dependence of CTI effects and allows us to separate the dependence on galaxy flux and size. Despite the similarity to the stellar model (B.5), we do not determine a common CTI model for the typically bright stars and faint galaxies, as a simple power law fit is not guaranteed to work well over such a wide range in S/N. Considering all selected COSMOS galaxies we determine best fitting parameters $(e_1^0, F, R, S) = (0.0230, 0.134, 0.638, 1.46)$. The correction for field distortion leads to a mean rotation of the original y-axis and hence readout direction in ACS stacks and *DRZ* exposures by $\phi \sim -2.5°$. Thus, CTE degradation has also a minor effect on the e_2 ellipticity component, which we account for in both the galaxy and stellar correction as $e_2^{\text{cte}} = \tan(2\phi)\,e_1^{\text{cte}} \simeq -0.087\,e_1^{\text{cte}}$. Note that CTI affects an image after convolution with the PSF. Thus, one would ideally wish to correct for it first. Yet, in order to determine the impact of CTI, we need to correct for PSF anisotropy first, which would otherwise dominate the mean e_1 ellipticity. We then subtract the CTI model (B.13) and compute the fully corrected galaxy ellipticity $e_\alpha^{\text{iso}} = (2/\text{Tr}[P^g])(e_\alpha^{\text{ani}} - e_\alpha^{\text{cti,gal}})$ with (B.3), which is an unbiased estimate for the shear g_α if (5), (6) are taken into account. As it may be easier applicable for non-KSB methods, we also quote best-fitting parameters $(e_1^0, F, R, S) = (0.0342, 0.068, 1.31, 1.26)$ if the actual shear estimates are fitted instead of the PSF anisotropy-corrected ellipticities, where the difference is caused by the PSF seeing correction blowing up the CTI ellipticity.

As a test for residual instrumental signatures we create a stacked shear catalogue from all COSMOS tiles. Doing this, we marginally detect a very weak residual shear pattern, which changes with cuts on $\overline{y_{1j}}$. To quantify and model this residual pattern, we fit it from the PSF anisotropy and CTI-corrected *galaxy* ellipticities with a focus-dependent, second-order model (B.12) jointly for all fields, yielding a very low rms ellipticity correction of ~ 0.003. One possible explanation for these residuals could be the limited capability of KSB+ to fully correct for a complex space-based PSF, despite the very good performance on the simulated data in Appendix B.2. Alternatively the limited number of stars per field may ultimately limit the possible PSF modelling accuracy. In order to assess if these residuals have any significant impact on our results, we have performed our science analysis twice, once with and once without subtraction of this residual model. The resulting changes in our constraints on σ_8 are at the 2% level, which is negligible compared to the statistical uncertainties. Also the E/B-mode decomposition is nearly unchanged (Fig. 4). We only detect a significant influence for the star-galaxy cross-correlation, which is strictly consistent with zero only if this correction is applied, but even without correction it is negligible compared to the expected cosmological signal (Fig. 5).

As last step in the catalogue preparation, we create a joint mosaic shear catalogue from all fields, carefully rejecting double detections in neighbouring tiles, where we keep the detection with higher S/N and refine relative shifts between tiles. In the case of close galaxy pairs with separations $<0\overset{''}{.}5$ we exclude the fainter component. Our filtered shear catalogue contains 472 991 galaxies, corresponding to 80 galaxies/arcmin^2, with a mean ellipticity dispersion per component $\sigma_{e,\alpha} = 0.31$. To limit the redshift extrapolation in Sect. 2.2.2, we apply an additional cut $i_{814} < 26.7$, leaving 446 934 galaxies, or 76 galaxies/arcmin^2.

We rotate all shear estimates to common coordinates, and accordingly create a joint mosaic star catalogue for the analysis in Sect. 4.

References

Albrecht, A., Amendola, L., Bernstein, G., et al. 2009 [arXiv:0901.0721]

Albrecht, A., Bernstein, G., Cahn, R., et al. 2006 [arXiv:astro-ph/0609591]

Allen, S. W., Rapetti, D. A., Schmidt, R. W., et al. 2008, MNRAS, 383, 879

Anderson, J. 2007, Instrument Science Rep. ACS 2007-08 (Baltimore: STScI), http://www.stsci.edu/hst/acs/documents/isrs/isr0708.pdf

Anderson, J., & King, I. R. 2006, Instrument Science Rep. ACS 2006-01 (Baltimore: STScI), http://www.stsci.edu/hst/acs/documents/isrs/isr0601.pdf

Bacon, D., Refregier, A., & Ellis, R. 2000, MNRAS, 318, 625

Bacon, D. J., Refregier, A., Clowe, D., & Ellis, R. S. 2001, MNRAS, 325, 1065

Bacon, D. J., Massey, R. J., Refregier, A. R., & Ellis, R. S. 2003, MNRAS, 344, 673

Bacon, D. J., Taylor, A. N., Brown, M. L., et al. 2005, MNRAS, 363, 723

Bartelmann, M., & Schneider, P. 2001, Phys. Rep., 340, 291

Benabed, K., & Bernardeau, F. 2001, Phys. Rev. D, 64, 083501

Benabed, K., & van Waerbeke, L. 2004, Phys. Rev. D, 70, 123515

Benitez, N. 2000, ApJ, 536, 571

Benjamin, J., Heymans, C., Semboloni, E., et al. 2007, MNRAS, 381, 702

Bergé, J., Amara, A., & Réfrégier, A. 2010, ApJ, 712, 992

Bernstein, G., & Jain, B. 2004, ApJ, 600, 17

Bertin, E., & Arnouts, S. 1996, A&AS, 117, 393

Brainerd, T., Blandford, R. D., & Smail, I. 1996, ApJ, 466, 623

Bridle, S., Balan, S. T., Bethge, M., et al. 2010, MNRAS, accepted [arXiv:0908.0945]

Brown, M. L., Taylor, A. N., Bacon, D. J., et al. 2003, MNRAS, 341, 100

Cappé, O., Douc, R., Guillin, A., Marin, J.-M., & Robert, C. 2008, Statistics and Computing, 18, 447

Chiaberge, M., Lian Lim, P., Kozhurina-Platais, V., Sirianni, M., & Mack, J. 2009, Instrument Science Rep. ACS 2009-01 (Baltimore: STScI), http://www.stsci.edu/hst/acs/documents/isrs/isr0901.pdf

Christensen, N., Meyer, R., Knox, L., & Luey, B. 2001, Classical and Quantum Gravity, 18, 2677

Coe, D., Benítez, N., Sánchez, S. F., et al. 2006, AJ, 132, 926

Cox, C., & Gilliland, R. L. 2002, in The 2002 HST Calibration Workshop (Baltimore: STScI), 58

Crittenden, R. G., Natarajan, P., Pen, U.-L., & Theuns, T. 2002, ApJ, 568, 20

de Bernardis, P., Ade, P. A. R., Bock, J. J., et al. 2000, Nature, 404, 955

Dodelson, S., Shapiro, C., & White, M. 2006, Phys. Rev. D, 73, 023009

Doré, O., Martig, M., Mellier, Y., et al. 2007, Phys. Rev. D, submitted [arXiv:0712.1599]

Dunkley, J., Komatsu, E., Nolta, M. R., et al. 2009, ApJS, 180, 306

Eifler, T., Schneider, P., & Hartlap, J. 2009, A&A, 502, 721

Eifler, T., Schneider, P., & Krause, E. 2010, A&A, 510, A7

Eisenstein, D. J., & Hu, W. 1998, ApJ, 496, 605

Eisenstein, D. J., Zehavi, I., Hogg, D. W., et al. 2005, ApJ, 633, 560

Erben, T., van Waerbeke, L., Bertin, E., Mellier, Y., & Schneider, P. 2001, A&A, 366, 717

Fernández-Soto, A., Lanzetta, K. M., & Yahil, A. 1999, ApJ, 513, 34

Freedman, W. L., Madore, B. F., Gibson, B. K., et al. 2001, ApJ, 553, 47

Fu, L., & Kilbinger, M. 2010, MNRAS, 401, 1264

Fu, L., Semboloni, E., Hoekstra, H., et al. 2008, A&A, 479, 9

Giannantonio, T., Scranton, R., Crittenden, R. G., et al. 2008, Phys. Rev. D, 77, 123520

Granett, B. R., Neyrinck, M. C., & Szapudi, I. 2008, ApJ, 683, L99

Hartlap, J., Simon, P., & Schneider, P. 2007, A&A, 464, 399

Hartlap, J., Schrabback, T., Simon, P., & Schneider, P. 2009, A&A, 504, 689

Heavens, A. 2003, MNRAS, 343, 1327

Heavens, A. F., Kitching, T. D., & Taylor, A. N. 2006, MNRAS, 373, 105

Heitmann, K., White, M., Wagner, C., Habib, S., & Higdon, D. 2010, ApJ, 715, 104

Hetterscheidt, M., Simon, P., Schirmer, M., et al. 2007, A&A, 468, 859

Heymans, C., Brown, M. L., Barden, M., et al. 2005, MNRAS, 361, 160

Heymans, C., Van Waerbeke, L., Bacon, D., et al. 2006a, MNRAS, 368, 1323

Heymans, C., White, M., Heavens, A., Vale, C., & van Waerbeke, L. 2006b, MNRAS, 371, 750

Hicken, M., Wood-Vasey, W. M., Blondin, S., et al. 2009, ApJ, 700, 1097

Hilbert, S., Hartlap, J., White, S. D. M., & Schneider, P. 2009, A&A, 499, 31

Hildebrandt, H., Wolf, C., & Benítez, N. 2008, A&A, 480, 703

Hildebrandt, H., Pielorz, J., Erben, T., et al. 2009, A&A, 498, 725

Hirata, C. M., Mandelbaum, R., Ishak, M., et al. 2007, MNRAS, 381, 1197

Hirata, C. M., & Seljak, U. 2004, Phys. Rev. D, 70, 063526

Ho, S., Hirata, C., Padmanabhan, N., Seljak, U., & Bahcall, N. 2008, Phys. Rev. D, 78, 043519

Hoekstra, H., Franx, M., Kuijken, K., & Squires, G. 1998, ApJ, 504, 636

Hoekstra, H., & Jain, B. 2008, Annual Review of Nuclear and Particle Science, 58, 99

Hoekstra, H., Mellier, Y., van Waerbeke, L., et al. 2006, ApJ, 647, 116

Hoekstra, H., Yee, H. K. C., & Gladders, M. D. 2002, ApJ, 577, 595

Hu, W. 1999, ApJ, 522, L21

Hu, W. 2002, Phys. Rev. D, 66, 083515

Hu, W., & Jain, B. 2004, Phys. Rev. D, 70, 043009

Huterer, D. 2002, Phys. Rev. D, 65, 063001

Huterer, D., & Linder, E. V. 2007, Phys. Rev. D, 75, 023519

Ilbert, O., Arnouts, S., McCracken, H. J., et al. 2006, A&A, 457, 841

Ilbert, O., Capak, P., Salvato, M., et al. 2009, ApJ, 690, 1236

Iocco, F., Mangano, G., Miele, G., Pisanti, O., & Serpico, P. D. 2009, Phys. Rep., 472, 1

Jain, B., & Taylor, A. 2003, Phys. Rev. Lett., 91, 141302

Jain, B., & Zhang, P. 2008, Phys. Rev. D, 78, 063503

Jarvis, M., & Jain, B. 2004, ApJ, submitted [astro-ph/0412234]

Jarvis, M., Bernstein, G. M., Fischer, P., et al. 2003, AJ, 125, 1014

Jarvis, M., Jain, B., Bernstein, G., & Dolney, D. 2006, ApJ, 644, 71

Jarvis, M., Schechter, P., & Jain, B. 2008, PASP, submitted [arXiv:0810.0027]

Jee, M. J., Blakeslee, J. P., Sirianni, M., et al. 2007, PASP, 119, 1403

Jee, M. J., Rosati, P., Ford, H. C., et al. 2009, ApJ, 704, 672

Joachimi, B., & Schneider, P. 2008, A&A, 488, 829

Joachimi, B., Schneider, P., & Eifler, T. 2008, A&A, 477, 43

Kaiser, N. 1992, ApJ, 388, 272

Kaiser, N., Squires, G., & Broadhurst, T. 1995, ApJ, 449, 460

Kaiser, N., Wilson, G., & Luppino, G. 2000 [arXiv:astro-ph/0003338]

Kilbinger, M., & Schneider, P. 2005, A&A, 442, 69

Kilbinger, M., Schneider, P., & Eifler, T. 2006, A&A, 457, 15

Kilbinger, M., Benabed, K., Guy, J., et al. 2009a, A&A, 497, 677

Kilbinger, M., Wraith, D., Robert, C. P., et al. 2009b, MNRAS, accepted [arXiv:0912.1614]

King, L., & Schneider, P. 2002, A&A, 396, 411

Kitching, T. D., Heavens, A. F., Taylor, A. N., et al. 2007, MNRAS, 138

Kitching, T. D., Taylor, A. N., & Heavens, A. F. 2008, MNRAS, 389, 173

Kitching, T. D., Amara, A., Abdalla, F. B., Joachimi, B., & Refregier, A. 2009, MNRAS, 1430

Koekemoer, A. M., Fruchter, A. S., Hook, R. N., & Hack, W. 2002, in The 2002 HST Calibration Workshop, ed. S. Arribas, A. Koekemoer, & B. Whitmore (Baltimore: STScI), 337

Koekemoer, A. M., Aussel, H., Calzetti, D., et al. 2007, ApJS, 172, 196

Komatsu, E., Dunkley, J., Nolta, M. R., et al. 2009, ApJS, 180, 330

Kowalski, M., Rubin, D., Aldering, G., et al. 2008, ApJ, 686, 749

Krause, E., & Hirata, C. M. 2009, A&A, submitted [arXiv:0910.3786]

Krist, J. 2003, Instrument Science Rep. ACS 2003-06 (Baltimore: STScI), http://www.stsci.edu/hst/acs/documents/isrs/isr0306.pdf

Lallo, M. D., Makidon, R. B., Casertano, S., & Krist, J. E. 2006, in SPIE Conf. Ser., 6270,

Leauthaud, A., Massey, R., Kneib, J.-P., et al. 2007, ApJS, 172, 219

Lilly, S. J., Le Fèvre, O., Renzini, A., et al. 2007, ApJS, 172, 70

Luppino, G. A., & Kaiser, N. 1997, ApJ, 475, 20

MacKay, D. J. 2003, Information Theory, Inference, and Learning Algorithms (Cambridge, UK: Cambridge University Press)

Mandelbaum, R., Hirata, C. M., Ishak, M., Seljak, U., & Brinkmann, J. 2006, MNRAS, 367, 611

Mandelbaum, R., Blake, C., Bridle, S., et al. 2009, MNRAS, submitted [arXiv:0911.5347]

Mantz, A., Allen, S. W., Ebeling, H., & Rapetti, D. 2008, MNRAS, 387, 1179

Mantz, A., Allen, S. W., Rapetti, D., & Ebeling, H. 2009, MNRAS, submitted [arXiv:0909.3098]

Massey, R., & Refregier, A. 2005, MNRAS, 363, 197

Massey, R., Refregier, A., Conselice, C. J., David, J., & Bacon, J. 2004, MNRAS, 348, 214

Massey, R., Refregier, A., Bacon, D. J., Ellis, R., & Brown, M. L. 2005, MNRAS, 359, 1277

Massey, R., Heymans, C., Bergé, J., et al. 2007a, MNRAS, 376, 13

Massey, R., Rhodes, J., Ellis, R., et al. 2007b, Nature, 445, 286

Massey, R., Rhodes, J., Leauthaud, A., et al. 2007c, ApJS, 172, 239

Massey, R., Stoughton, C., Leauthaud, A., et al. 2010, MNRAS, 401, 371

McDonald, P., Trac, H., & Contaldi, C. 2006, MNRAS, 366, 547

Miralles, J.-M., Erben, T., Hämmerle, H., et al. 2005, A&A, 432, 797

Mobasher, B., Capak, P., Scoville, N. Z., et al. 2007, ApJS, 172, 117

Munshi, D., Valageas, P., van Waerbeke, L., & Heavens, A. 2008, Phys. Rep., 462, 67

Mutchler, M., & Sirianni, M. 2005, Instrument Science Rep. ACS 2005-03 (Baltimore: STScI), http://www.stsci.edu/hst/acs/documents/isrs/isr0503.pdf

Nakajima, R., Bernstein, G. M., Fadely, R., Keeton, C. R., & Schrabback, T. 2009, ApJ, 697, 1793

Peacock, J., Schneider, P., Efstathiou, G., et al. 2006, Fundamental Cosmology, ESA-ESO Working Groups Report No. 3 http://www.stecf.org/coordination/esa_eso/cosmology.php

Percival, W. J., Cole, S., Eisenstein, D. J., et al. 2007, MNRAS, 381, 1053

Percival, W. J., Reid, B. A., Eisenstein, D. J., et al. 2009, MNRAS, 1741

Perlmutter, S., Aldering, G., Goldhaber, G., et al. 1999, ApJ, 517, 565

Refregier, A., & Bacon, D. 2003, MNRAS, 338, 48

Refregier, A., Rhodes, J., & Groth, E. J. 2002, ApJ, 572, L131

Refregier, A., Amara, A., Kitching, T., & Rassat, A. 2008, A&A, submitted [arXiv:0810.1285]

Rhodes, J., Refregier, A., Collins, N. R., et al. 2004, ApJ, 605, 29

Rhodes, J. D., Massey, R. J., Albert, J., et al. 2007, ApJS, 172, 203

Riess, A. G., Filippenko, A. V., Challis, P., et al. 1998, AJ, 116, 1009

Riess, A. G., Strolger, L.-G., Casertano, S., et al. 2007, ApJ, 659, 98

Riess, A. G., Macri, L., Casertano, S., et al. 2009, ApJ, 699, 539

Rudd, D. H., Zentner, A. R., & Kravtsov, A. V. 2008, ApJ, 672, 19

Schimd, C., Tereno, I., Uzan, J., et al. 2007, A&A, 463, 405

Schlegel, D. J., Finkbeiner, D. P., & Davis, M. 1998, ApJ, 500, 525

Schmidt, F. 2008, Phys. Rev. D, 78, 043002

Schneider, P. 1996, MNRAS, 283, 837

Schneider, P. 2006, in: Gravitational Lensing: Strong, Weak & Micro, Saas-Fee Advanced Course 33, Swiss Society for Astrophysics and Astronomy, ed. G. Meylan, P. Jetzer, & P. North (Berlin: Springer-Verlag), 269

Schneider, P., & Kilbinger, M. 2007, A&A, 462, 841

Schneider, P., van Waerbeke, L., Jain, B., & Kruse, G. 1998, MNRAS, 296, 873

Schneider, P., van Waerbeke, L., & Mellier, Y. 2002, A&A, 389, 729

Schrabback, T., Erben, T., Simon, P., et al. 2007, A&A, 468, 823

Scoville, N., Abraham, R. G., Aussel, H., et al. 2007a, ApJS, 172, 38

Scoville, N., Aussel, H., Benson, A., et al. 2007b, ApJS, 172, 150

Semboloni, E., Mellier, Y., van Waerbeke, L., et al. 2006, A&A, 452, 51

Semboloni, E., van Waerbeke, L., Heymans, C., et al. 2007, MNRAS, 375, L6

Semboloni, E., Tereno, I., van Waerbeke, L., & Heymans, C. 2009, MNRAS, 397, 608

Semboloni, E., Schrabback, T., Van Waerbeke, L., et al. 2010, MNRAS, submitted

Shapiro, C. 2009, ApJ, 696, 775

Simon, P., King, L. J., & Schneider, P. 2004, A&A, 417, 873

Smith, R. E., Peacock, J. A., Jenkins, A., et al. 2003, MNRAS, 341, 1311

Spergel, D. N., Verde, L., Peiris, H. V., et al. 2003, ApJS, 148, 175

Springel, V., White, S. D. M., Jenkins, A., et al. 2005, Nature, 435, 629

Suyu, S. H., Marshall, P. J., Auger, M. W., et al. 2010, ApJ, 711, 201

Takada, M., & Jain, B. 2004, MNRAS, 348, 897

Taylor, A. N., Kitching, T. D., Bacon, D. J., & Heavens, A. F. 2007, MNRAS, 374, 1377

Vafaei, S., Lu, T., van Waerbeke, L., et al. 2010, Astrop. Phys., 32, 340

Van Waerbeke, L., Mellier, Y., Erben, T., et al. 2000, A&A, 358, 30

Van Waerbeke, L., Mellier, Y., & Hoekstra, H. 2005, A&A, 429, 75

Vikhlinin, A., Kravtsov, A. V., Burenin, R. A., et al. 2009, ApJ, 692, 1060

Wittman, D. M., Tyson, J. A., Kirkman, D., Dell'Antonio, I., & Bernstein, G. 2000, Nature, 405, 143

Wraith, D., Kilbinger, M., Benabed, K., et al. 2009, Phys. Rev. D, 80, 023507